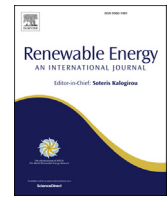




ELSEVIER

Contents lists available at ScienceDirect

Renewable Energy

journal homepage: www.elsevier.com/locate/renene

OC6 phase I: Improvements to the OpenFAST predictions of nonlinear, low-frequency responses of a floating offshore wind turbine platform

Lu Wang ^{*}, Amy Robertson, Jason Jonkman, Yi-Hsiang Yu ¹

National Renewable Energy Laboratory, 15013 Denver W. Pkwy, Golden, CO, 80401, USA



ARTICLE INFO

Article history:

Received 5 August 2021

Received in revised form

11 December 2021

Accepted 14 January 2022

Available online 24 January 2022

Keywords:

Offshore wind

Semisubmersible

Low frequency

Resonance

OpenFAST

OC6

ABSTRACT

In the OC5 and OC6² projects, the authors observed a persistent underprediction of the nonlinear, low-frequency responses of an offshore wind semisubmersible with many mid-fidelity engineering models, including the OpenFAST tool developed by the National Renewable Energy Laboratory. Both the low-frequency wave excitation in surge and pitch and the resulting resonance motions were severely underpredicted. In response, we developed several modifications to the OpenFAST model from the OC5/6 projects to improve the predictions of the low-frequency wave loads and responses. All modifications are in the modeling of the viscous drag forces. Efforts were made to provide physical justifications to the changes and to limit the number of additional parameters requiring tuning, so that the modified model can be applied to other floating wind systems. With the proposed modifications, the predictions of the low-frequency surge and pitch wave loads on a fixed floater and the resonance responses of a floating structure are both significantly improved with a single set of model coefficients, which leads to good agreement with the measurements from the OC6 wave-basin experimental campaign.

© 2022 Elsevier Ltd. All rights reserved.

1. Introduction

During the past Offshore Code Comparison Collaboration, Continued with Correlation (OC5) project under the International Energy Agency Wind Task 30 framework—a project focused on the validation of the coupled modeling tools used to design and analyze floating offshore wind turbine systems—it was discovered that most state-of-the-art, mid-fidelity models based on the Morison equation and/or the potential-flow theory underpredicted the loads and motion of a semisubmersible offshore wind platform under both wind-wave and wave-only conditions [1]. The most significant underprediction occurred at low frequencies, outside the range of linear wave excitation. Nonlinear, low-frequency wave excitation leads to surge and pitch resonance motion of the structure, causing high loads. The underprediction of the low-frequency response can therefore be attributed to an underprediction of the

nonlinear wave excitation and/or overprediction of the hydrodynamic damping at the surge and pitch resonance frequencies.

Extensive study of the low-frequency responses of floating wind semisubmersibles has been carried out. The experimental investigation by do Carmo et al. [2] investigated the forced-oscillation, free-decay, and slow-drift motions of a semisubmersible offshore wind platform. The calm-water free-decay experiments and forced-oscillation experiments led to different surge damping values, with those from forced oscillation being consistently lower; however, even with the lower damping coefficient from forced oscillation, the potential-flow model still underpredicted the slow-drift motion, corroborating the trend identified in OC5 [1]. This observation also suggests that the underprediction of low-frequency wave excitation must play a role in the overall underprediction of the response, at least in surge. The substantial underprediction of the nonlinear, difference-frequency surge force on another offshore wind semisubmersible by full second-order potential-flow quadratic transfer functions (QTFs) was confirmed in an experimental campaign with a fixed model in bichromatic waves by Lopez-Pavon et al. [3], even with the wave amplitudes deliberately kept low to reduce viscous effects. This underprediction of the low-frequency response has also been observed by many other researchers [4,5].

To better understand and address this underprediction, Phase I of the present OC6 (OC5 with unCertainty) project organized a

^{*} Corresponding author.

E-mail address: Lu.Wang@nrel.gov (L. Wang).

¹ Present address: Department of Civil Engineering, National Yang Ming Chiao Tung University, No. 1001, Daxue Rd., East District, Hsinchu City, Taiwan, 30010.

² Offshore Code Comparison Collaboration, Continued with Correlation (OC5) and OC6 (OC5 with unCertainty) are both projects under the International Energy Agency Wind Task 30 framework.

three-way validation study into the low-frequency responses of the OC6-DeepCwind semisubmersible with new wave-basin experiments [6–8] and numerical investigations with both mid-fidelity engineering tools [9] and high-fidelity computational fluid dynamics (CFD) simulations [10–12]. The experimental setups with the OC6-DeepCwind semisubmersible are shown in Fig. 1. With the fixed configuration (Fig. 1a), the floater was restrained, and the wave loads on the structure were measured. With the floating configuration in Fig. 1b, the wave-induced motion of the floater was measured instead. The tools used in the study of [9] include a range of mid-fidelity models based on the Morison equation with a strip-theory formulation, potential-flow solutions, or a combination of both, such as the OpenFAST model developed by the National Renewable Energy Laboratory (NREL). The NREL OpenFAST tool models the floater in the time domain and incorporates both the first- and second-order frequency-domain potential-flow solutions to model the wave excitation and radiation loads. In addition to a global linear damping matrix, the OpenFAST model also evaluates quadratic drag forces based on empirical drag coefficients to model the viscous effects. Distributed transverse drag is evaluated along the various members of the floater following a strip-theory-type formulation, and lumped drag forces in the normal directions are also evaluated on the faces of the heave plates. The collaborative study of [9] with the engineering models, which involved more than two dozen organizations submitting results from different state-of-the-art tools, showed again that all models underpredicted, to varying degrees, both the low-frequency wave excitation on a fixed structure and the motion of a freely floating structure. The CFD simulations, on the other hand, tend to provide better predictions of the low-frequency wave excitation when compared to the experiment [12], suggesting CFD results can be used to further study the underprediction issue and provide reference data for tuning the engineering models in lieu of, or in addition to, the wave-basin experiments.

At the low surge and pitch resonance frequencies, viscous damping generally dominates over wave radiation damping [13]; therefore, most effort to address the underprediction of low-frequency responses has focused on improving the tuning of the viscous drag coefficients used by the models. In the OC6 Phase I investigation with engineering models [9], a consistent trend was observed in which higher transverse Morison drag coefficients increased the predicted low-frequency surge force on a fixed floater, leading to better agreement with the experiment. The free-decay motion of the structure was also better predicted; however, the increased drag also decreased the motion response of the system under irregular wave excitation, exacerbating the underprediction. The same observation was also made by Lemmer et al.

[14], who showed that the best drag coefficient for free-decay motion was 3–5 times that for wave conditions. This conflict can be resolved with the help of a depth-dependent transverse drag coefficient [15–17], which is further explored in the present study. Böhm et al. [18] systematically tuned the transverse drag coefficient for the columns and the axial/normal drag coefficient for the heave plates for an OpenFAST model of the OC6-DeepCwind semi-submersible using a global pattern search algorithm. A single heave-plate axial drag coefficient was used, which simultaneously affected the heave and pitch responses of the structure. The outcome of the optimization clearly indicated that no single value of the heave-plate drag coefficient can provide acceptable predictions for both heave and pitch motions. It was conjectured that the existing OpenFAST model was unable to represent pitch damping well. With two separate optimization searches, one based on surge and heave motion and the other on pitch motion only, the results showed that the axial drag coefficient for the heave plates that worked best for heave motion was approximately double that for pitch, rendering a compromise impossible. Lemmer et al. [14] argued that heave motion is less important for floating wind turbines and tuned the axial drag coefficients of the heave plates based on pitch motion only. In general, it is possible to obtain good agreement between the model and the experiment for selected low-frequency responses by specifically tuning the drag coefficients against them as demonstrated by Simos et al. [19] and Pegalajar-Jurado and Bredmose [20] with the slow drift motion, but it is challenging to simultaneously obtain satisfactory predictions of all low-frequency response metrics of interest with the same set of model coefficients, even just for a single wave condition. To achieve this, some modifications to the modeling practice and model formulation are required. One notable approach aimed at improving the predictions of low-frequency wave excitation and floater response is the QTF-correction method of Li and Bachynski-Polić [21]. With this method, the difference-frequency QTFs for the wave excitation on a fixed structure from second-order potential-flow theory are modified and scaled up based on the results from a series of CFD simulations with bichromatic-incident waves. The modified QTFs are subsequently used as inputs to a mid-fidelity engineering model, improving the predictions of the nonlinear, low-frequency wave loads on a fixed structure [21]. Subsequent application of the modified QTFs in the modeling of the same structure under a floating condition also led to improved predictions of the low-frequency resonance motion [22].

In this article, we propose a different approach to address the underprediction of the nonlinear, low-frequency wave loads and responses by mid-fidelity tools. Instead of modifying the QTFs, we devised three modifications to the empirical drag forces in the

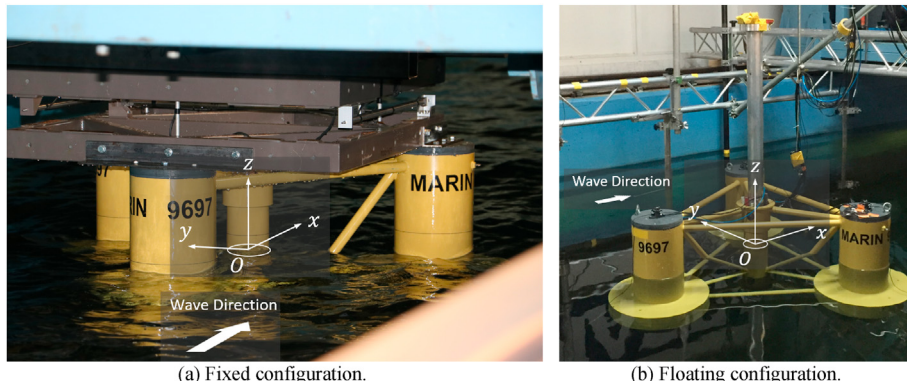


Fig. 1. Setups of (a) the fixed configuration and (b) the freely floating configuration of the DeepCwind floating wind semisubmersible of the OC6 Phase Ia model experiment campaign at the concept basin of the Maritime Research Institute Netherlands (MARIN). Photo by Amy Robertson, NREL.

existing OpenFAST model developed by NREL for the OC5/6 projects [9]. The modifications are inspired by the data and observations gathered throughout the OC6 Phase I project. Although there are potentially many possible approaches to obtain improved low-frequency predictions, at least for a given wave condition and geometry, we strived to formulate modifications that are physically justifiable and general without substantially increasing the difficulty of model tuning. Note that we primarily focused on the responses of the structure in waves. The behaviors of the structure in calm water, such as free decay and forced oscillation, were not explicitly considered; however, we kept the model coefficients from our original OpenFAST model [9], which were tuned against free-decay motion [18], to retain the calm-water characteristics of the model as much as possible. The improved model described here is one of the principal outcomes of the OC6 Phase I project.

The physical problem investigated in this article is described in Section 2. The original OpenFAST model developed for OC5/6 by NREL [9] is described in detail in Section 3 for reference and to illustrate the underprediction of low-frequency wave loads and motion response encountered in the OC5 Phase II [1] and OC6 Phase I projects [9]. Several proposed modifications to this original model are discussed in Section 4 to address the underpredictions. The proposed modified model is validated with a different wave condition in Section 5 followed by additional discussions and recommendations for future applications in Section 6. Finally, the conclusions are provided in Section 7.

2. Problem description

The physical setup adopted for the present study closely follows the experimental campaign within OC6 Phase Ia [6,23], which included both a floating configuration with a simplified rigid tower and block mass to represent the wind turbine and a constrained condition with the substructure only (see Fig. 1). The experiments were performed at 1:50 model scale; however, all dimensional values in the present article are presented at full scale based on Froude scaling. The semisubmersible design has the same geometry and draft as the OC5-DeepCwind semisubmersible [1] but slightly modified mass and inertia properties.

The semisubmersible in the equilibrium position, along with the adopted coordinate system, is shown in Fig. 2a. The platform is oriented such that a single upstream outer column faces the incident waves, and the two remaining outer columns are downstream on the port and starboard sides. The water depth is uniformly 180 m, and the gravitational acceleration is taken as $g = 9.81 \text{ m/s}^2$. A saltwater density of $\rho = 1,025 \text{ kg/m}^3$ is used.

A global earth-fixed coordinate system, Oxyz, is adopted with the xy-plane coinciding with the calm-water surface. The origin, O,

is on the centerline of the central main column in the equilibrium position, and the +x-axis points along the direction of wave propagation. Because of port-starboard symmetry, the motion of the platform is primarily in the vertical xz-plane. For the fixed condition, the wave-induced surge and heave forces are in the x- and z-directions, respectively, and the pitch moment is computed about the y-axis. For the freely floating condition, the translation of the floater is defined by the position of the body-fixed floater reference point, which coincides with the origin at equilibrium, in the earth-fixed coordinate system. The pitch motion is again about the y-axis.

The combined dynamic properties of the semisubmersible, rigid tower, and wind turbine (represented by a block mass in the experiment) and the mooring setup for the freely floating configuration are given in Table 1 [6]. The three taut mooring lines connected to the heave plates (shown in Fig. 2b) are treated as thin and massless linear springs. This is consistent with the actual experimental setup, which used thin, taut wires as mooring lines. The wires went through a pulley system to connect to soft springs above water. This simplified mooring setup was adopted by the experimental campaign specifically to minimize uncertainty and facilitate numerical modeling.

The floater is subjected to long-crested, irregular incident waves in the +x-direction. Two wave spectra are considered: Joint North Sea Wave Project (JONSWAP) and white noise. The wave conditions are listed in Table 2. In the OC6 project, the same JONSWAP wave spectrum is used for both Load Case (LC) 3.3 and LC 5.3 with the former having a fixed floater and the latter a freely floating structure. The white-noise wave is used for LC 3.4 and LC 5.4, again with the former denoting a fixed condition and the latter a freely floating condition. For convenience, two frequency ranges are defined for each wave condition in Table 2: a wave-frequency range dominated by the linear excitation from the incident waves and a low-frequency range primarily containing nonlinear, difference-frequency excitation.

In the current article, the OC6 project numbering of the load cases is used for brevity. To facilitate validation against wave-basin experiments, the experimentally measured wave-elevation time series are used directly as inputs to the OpenFAST simulations to avoid issues with statistical convergence.

3. The underprediction of low-frequency responses by OpenFAST

This article focuses on improving the ability of OpenFAST to predict the low-frequency responses of the offshore wind semisubmersible, including both the nonlinear, low-frequency wave excitation and the surge and pitch resonance motion of the

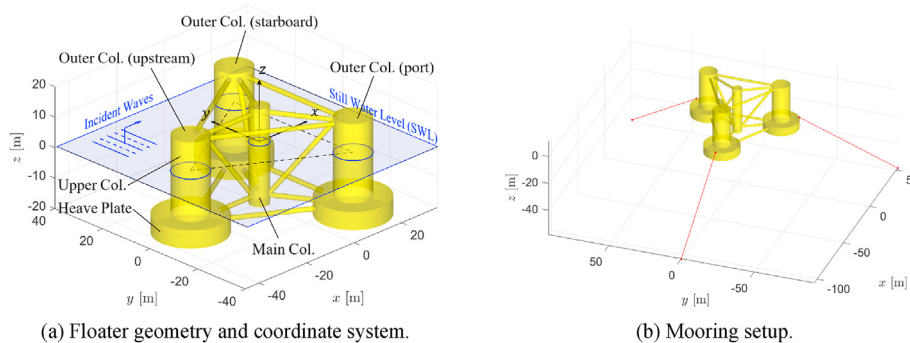


Fig. 2. Schematics of the physical setup. (a) Geometry of the OC6-DeepCwind semisubmersible and the adopted coordinate system for both the fixed and the freely floating configurations. (b) The taut-spring mooring setup for the floating configuration.

Table 1

Combined floater, tower, and turbine dynamic properties and the mooring setup of the freely floating OC6-DeepCwind semisubmersible floating offshore wind turbine [6].

Properties	Values																
Structure Dynamic Properties																	
Mass (m)	1.4196×10^7 kg																
Displace Volume (\forall)	14,053 m ³																
Vertical Center of Mass (G_z)	-7.32 m																
Vertical Center of Buoyancy (B_z)	-13.15 m																
Pitch Moment of Inertia about Center of Mass (I_{yy})	1.2979×10^{10} kg m ²																
Surge Natural Period	105 s																
Heave Natural Period	17.2 s																
Pitch Natural Period	31.0 s																
Mooring																	
Unstretched line length (l_0)	55.432 m																
Linear spring constant (k)	4.89×10^4 N/m																
Fairleads at Equilibrium and Anchors																	
Fairleads	<table> <tr> <th></th> <th>x [m]</th> <th>y [m]</th> <th>z [m]</th> </tr> <tr> <td>Upstream Column</td> <td>-40.870</td> <td>0.00</td> <td>-14.00</td> </tr> <tr> <td>Starboard Column</td> <td>20.434</td> <td>35.39</td> <td>-14.00</td> </tr> <tr> <td>Port Column</td> <td>20.434</td> <td>-35.39</td> <td>-14.00</td> </tr> </table>		x [m]	y [m]	z [m]	Upstream Column	-40.870	0.00	-14.00	Starboard Column	20.434	35.39	-14.00	Port Column	20.434	-35.39	-14.00
	x [m]	y [m]	z [m]														
Upstream Column	-40.870	0.00	-14.00														
Starboard Column	20.434	35.39	-14.00														
Port Column	20.434	-35.39	-14.00														
Anchors	<table> <tr> <th></th> <th>x [m]</th> <th>y [m]</th> <th>z [m]</th> </tr> <tr> <td>Upstream Column</td> <td>-105.47</td> <td>0.00</td> <td>-58.40</td> </tr> <tr> <td>Starboard Column</td> <td>52.73</td> <td>91.34</td> <td>-58.40</td> </tr> <tr> <td>Port Column</td> <td>52.73</td> <td>-91.34</td> <td>-58.40</td> </tr> </table>		x [m]	y [m]	z [m]	Upstream Column	-105.47	0.00	-58.40	Starboard Column	52.73	91.34	-58.40	Port Column	52.73	-91.34	-58.40
	x [m]	y [m]	z [m]														
Upstream Column	-105.47	0.00	-58.40														
Starboard Column	52.73	91.34	-58.40														
Port Column	52.73	-91.34	-58.40														

Table 2

Incident wave conditions for both the fixed and the freely floating conditions.

Wave Conditions	Properties				
JONSWAP: LC 3.3 (fixed condition) and LC 5.3 (freely floating condition)	Significant Wave Height 7.4 m	Peak Period 12.0 s	Peak Enhancement Factor, Low-Freq. Range γ 3.3	Range 0.005–0.05 Hz	Wave-Freq. Range 0.0552 -0.1345 Hz
White Noise: LC 3.4 (fixed condition) and LC 5.4 (freely floating condition)	Significant Wave Height 6.7 m	Start Period 6.0 s	End Period 26.0 s	Low-Freq. Range 0.005 0.0385 -0.036 Hz	Wave-Freq. Range 0.0385 -0.1667 Hz

structure. Both wave excitation and floater motion were severely underpredicted by the NREL OpenFAST model developed for the OC6 Phase Ia project (referred to as the “original” model in this article) and other mid-fidelity engineering-level tools for floating offshore wind systems [1,9]. To provide a background and baseline for the present investigation, the original NREL OpenFAST model used by Robertson et al. [9] is described here with the simulation results demonstrating the underprediction of the low-frequency responses. This underprediction is addressed with several modifications to the original model as described in Section 4.

3.1. Original OC6 OpenFAST model

The original OC6 OpenFAST model developed at NREL [9] simulates the hydrodynamics of the offshore wind semisubmersible in the time domain using a combination of second-order potential-flow theory and empirical drag forces. The frequency-domain linear potential-flow solution, including linear wave excitation, added mass, wave damping, and hydrostatic stiffness, was obtained using the commercial potential-flow, boundary-element solver WAMIT V6.1 [24]. The second-order potential-flow problem was solved using WAMIT V6.107S to obtain the sum- and difference-frequency wave-excitation QTFs. Because the second-order solution also depends on the first-order motion response amplitude operators, two different sets of QTFs were computed for the fixed and freely floating conditions. The use of full second-order QTFs was identified as one of the model components that consistently improves the prediction of low-frequency structural responses and, therefore, must be included in the simulation [9]. Replacing the full QTFs with Newman’s approximation will lead to further underprediction [3,9,19]. The first-order wave-radiation forces and moments are

computed using the time convolution of the body velocities and the radiation impulse-response function [25].

Two types of empirical drag force are included: distributed transverse drag force perpendicular to the column and heave-plate centerlines, and lumped axial/normal drag forces on the two faces of the heave plates. As shown in Fig. 3, the columns and the heave plates are represented in OpenFAST by line segments along the centerline of each member for the purpose of computing the

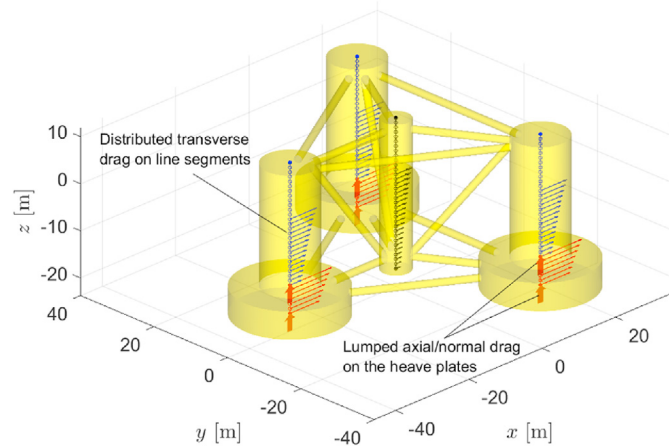


Fig. 3. Distributed transverse drag forces and the lumped axial/normal drag forces in the OpenFAST model. The horizontal arrows represent the distributed transverse drag forces evaluated and applied along the centerlines of the columns and heave plates. The large vertical arrows represent the lumped axial/normal drag forces evaluated and applied at the end nodes of the heave plates located at the centers of the top and bottom faces of the heave plates.

distributed transverse drag force. Each line segment is 1 m long, and the transverse drag force, \mathbf{F}_D , per unit length is computed at the end points of each segment using Eq. (1) [26]:

$$\mathbf{F}_D = \frac{1}{2} C_D \rho (2R) |\mathbf{v}_r - (\mathbf{v}_r \cdot \mathbf{k}) \mathbf{k}| (\mathbf{v}_r - (\mathbf{v}_r \cdot \mathbf{k}) \mathbf{k}), \quad (1)$$

where \mathbf{v}_r is the velocity vector of the incident wave field relative to the body velocity at the segment end points, \mathbf{k} is the unit vector in the direction of the segment, R is the radius of the column or heave plate, and C_D is the drag coefficient. A drag coefficient of $C_D = 0.4$ is used for the upper columns and the main column, and $C_D = 1.6$ is used for the heave plates. These values were obtained by tuning the model to match the experimental surge, heave, and pitch free-decay motions [18]. The lower value of $C_D = 0.4$ for the upper columns is consistent with the drag coefficient recommended by Lemmer et al. [14] for vertical cylinders, and the increased value of $C_D = 1.6$ for the heave plates is justified by the presence of sharp corners and strong flow separation.

The total transverse drag force and the resulting moment are obtained by integrating the distributed force along the line segments. On the upper columns and the main column, the transverse drag force is integrated up to the instantaneous first-order free surface with vertical wave stretching; that is, the wave kinematics above the still water level is assumed to be the same as that at the still water level.³ The drag force above the instantaneous free surface is zero. The slender braces and pontoons connecting the columns and the heave plates can also be included when calculating the distributed drag force; however, because of the small diameter, their contribution to the total wave loads and effects on the floater motion is negligible. (Note that the slender braces and pontoons were included when solving the first-order potential-flow solution but omitted when solving the second-order problem, as was done in Ref. [27], because of their small diameter relative to the characteristic incident wavelength.) All results shown in the present article were therefore obtained with the slender connecting members omitted from the drag calculation.

In addition to the distributed transverse drag, the lumped axial/normal drag forces perpendicular to the top and bottom faces of the heave plates are applied to the end nodes of the heave plates (see Fig. 3). The axial drag force, $\mathbf{F}_{D_{Ax}}$, is given by Eq. (2) [26] (a coefficient of 1/4 is used in place of the usual 1/2 because half of the total drag force is applied to each side of the heave plate):

$$\mathbf{F}_{D_{Ax}} = \frac{1}{4} C_{D_{Ax}} \rho \mathbf{A} |\mathbf{v}_{r,n} | \mathbf{v}_{r,n}, \quad (2)$$

where \mathbf{A} is the normal directional face area of the heave plates pointing away from the heave plates, and

$$\mathbf{v}_{r,n} = (\mathbf{v}_r \cdot \mathbf{A}) / |\mathbf{A}|. \quad (3)$$

In Eq. (3), \mathbf{v}_r is the velocity vector of the incident wave field relative to the local body velocity at the end nodes of the heave plates, and $\mathbf{v}_{r,n}$ is the component of \mathbf{v}_r normal to the top or bottom faces of the heave plates. Note that $\mathbf{v}_{r,n}$ is positive when the normal component of the relative flow velocity points away from the heave plate. For simplicity, the area of the bottom face of the heave plate is used for both the top face and the bottom face. The lumped axial drag force is controlled by the axial drag coefficient, $C_{D_{Ax}}$, to which a value of 4.1 is assigned for both faces despite the presence of the upper column above the heave plate. This is because Zhang and Ishihara

[28] showed that, for a similar column/heave plate geometry, the heave-plate drag coefficient remains approximately constant when the ratio of the heave-plate diameter to the upper-column diameter is greater than 2 (this ratio is exactly 2 for the present geometry), suggesting limited influence from the presence of the upper column; therefore, it is physically justifiable to use the same reference area and drag coefficient for both the top and bottom faces of the heave plates for the present geometry. The drag coefficient of 4.1 was again tuned based on free-decay experiments [18]. (In Refs. [9,18], the doubled axial drag coefficient of 8.2 was reported. This is because the drag force was only applied to the bottom face of the heave plates, which led to results effectively identical to Fig. 4 obtained with the drag force applied to both the top and bottom faces but with half the drag coefficient, 4.1.) The relatively low $C_{D_{Ax}}$ is a consequence of the large thickness of the heave plates; the drag coefficient of heave plates tends to decrease with an increasing thickness-to-diameter ratio [28]. Note that different combinations of the face area and drag coefficients can be used to obtain effectively identical results. For example, if the actual smaller area of the top face of the heave plate is used, a larger drag coefficient can be assigned to the top face compared to that for the bottom face to obtain the same result. The axial drag on the bottom of the main column has little effect on the floater response because of the much smaller area relative to the heave plates; therefore, this force is neglected.

For the freely floating condition, the OpenFAST simulations have full six-degrees-of-freedom structural motion, but only surge, heave, and pitch motions are excited because of port-starboard symmetry. In addition to the wave-radiation damping and the distributed/lumped drag, global linear damping coefficients of 75 kN s/m in surge and 31 MN·m s/rad in pitch are included in the model following [9,18]. The added damping provides the correct linear damping characteristics of the model during small-amplitude free-decay oscillation. For the sake of consistency with past investigations and to retain the model characteristics in calm water, the added damping is retained in the present investigation.

3.2. The underprediction of low-frequency responses by the original OC6 model

To demonstrate the underprediction identified in Refs. [1,9], we first consider the JONSWAP irregular waves described in Table 2. The wave loads on the offshore wind platform when constrained (LC 3.3) and the motion of the platform when freely floating (LC 5.3) are computed using the original OpenFAST model described in Section 3.1. The resulting power spectral densities (PSDs) are shown in Fig. 4. Whereas the model generally predicts the wave-frequency (blue regions in Fig. 4) responses of the structure well, the OpenFAST model severely underpredicts the surge force when compared to the experiment by almost one order of magnitude in the low-frequency region (the pink region in Fig. 4a). While not as severe, the low-frequency pitch moment (Fig. 4b) is also consistently underpredicted by the model by approximately 17% (which corresponds to a 30% underprediction of the pitch moment PSD). The underpredicted low-frequency wave load from OpenFAST is at least partially responsible for the underprediction of the low-frequency surge and pitch resonance motions (Fig. 4c and d); the overprediction of the damping or drag in surge and pitch might also play a role.

The underprediction of the low-frequency loads and responses is not unique to OpenFAST. It was observed, to varying degrees, for a host of state-of-the-art, mid-fidelity engineering-level tools from more than two dozen academic and research institutions and industry partners [9,29]. The error in the model predictions resulted in a 10%–20% underprediction of the global ultimate and fatigue

³ The wave-stretching capability is not available in the current publicly released version of OpenFAST; a separate development version was used in this study.

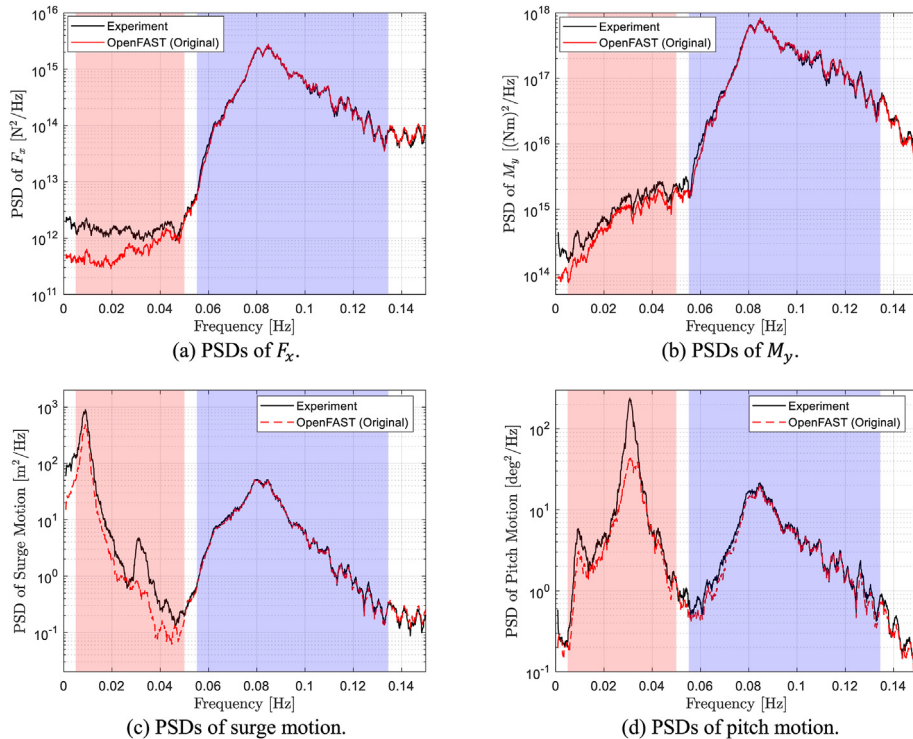


Fig. 4. Power spectral densities (PSDs) of the wave-induced (a) surge force, F_x , and (b) pitch moment, M_y , on the DeepCwind offshore wind platform when constrained (LC 3.3), and PSDs of (c) surge motion and (d) pitch motion of the platform when freely floating (LC 5.3). The pink region indicates the low-frequency range, and the blue region is the wave-frequency range (see Table 2). The original OpenFAST model of [9] is described in Section 3.1.

loads [1]; therefore, the engineering models cannot reliably be used for design optimization purposes. The current article focuses on addressing this limitation of the engineering models to obtain better predictions in the low-frequency region.

4. Modifications to the original OpenFAST model to improve low-frequency predictions

In this section, we propose several modifications to the modeling practice and model formulation of OpenFAST to address the deficiencies of the original OC6 model described in Section 3. There are, of course, multiple ways to achieve better agreement with the experiment. For instance, as proposed in Ref. [9], we can artificially modify and scale up the QTFs from the second-order potential-flow theory to increase the difference-frequency wave excitation without changing the wave-frequency responses. This has been applied to a fixed structure to good effect by Li and Bachynski-Polić [21]; however, this approach also leads to substantial challenges with model tuning. It is difficult to know how we should modify the QTFs without extensive a priori knowledge of the system behavior from either wave-basin experiments or CFD simulations; therefore, in this article we attempt to devise modifications to the original model that are physically justifiable and, ideally, that also have minimal complexity to avoid further complicating model tuning as much as possible. Finally, we would like to have a reasonably general model that applies to a range of similar wave conditions and floater configurations, including both fixed and freely floating, without extensive retuning of the model.

A PSD-integral metric, S_{int} , is used to quantitatively gauge the agreement between the OpenFAST predictions and the experimental measurements [9]:

$$S_{int} = \int_{f_0}^{f_1} S(f) df, \quad (4)$$

where $S(f)$ is the one-sided, unsmoothed, PSD of any quantity of interest (force, moment, motion, and so on). The integration over frequency, f , is performed over either the low-frequency range or the wave-frequency range specified in Table 2 for each wave condition. For consistency, all PSDs and PSD integrals shown in this article were computed from the same 3-h time window after an initial transient phase was removed. The PSD integral can be thought of as the standard deviation of the quantity of interest over a given frequency range.

The uncertainties in S_{int} were also recomputed for the experimental results following the procedure described in Ref. [6] to facilitate comparison with model predictions. In Ref. [6], eight physical parameters in the experiment with significant levels of systematic uncertainty were identified that potentially had non-negligible effects on the response metric S_{int} : wave excitation, longitudinal and vertical positions of the center of mass of the physical model, pitch moment of inertia, column/heave plate diameter, model draft, model mass, and the mooring spring constant. The estimated experimental uncertainties of these parameters were propagated to S_{int} using numerical models and combined in quadrature, assuming independent sources of error to obtain the total experimental uncertainties; however, in contrast to Ref. [6], which used four different mid-fidelity engineering models to propagate the uncertainty, only the final improved OpenFAST model described in this article was used to propagate the uncertainties here. Furthermore, the random uncertainty in the experimental results, which was found to be negligible compared to the systematic part [6], is neglected.

4.1. Wave stretching and depth-dependent transverse drag coefficient

We first focus on the underprediction of the low-frequency surge force on the fixed structure (LC 3.3). As part of OC6 Phase I, a coordinated investigation with both high-fidelity CFD simulations and wave-basin experiments was carried out to better understand the nonlinear, difference-frequency wave excitation on a constrained offshore wind semisubmersible in bichromatic waves [10–12] using a similar floater geometry. During this study, we identified that near the surge resonance frequency (0.01 Hz) of the structure, the nonlinear surge force primarily comes from the viscous drag on the structure, whereas second-order wave diffraction has negligible contribution. Based on this observation, we focus on the transverse drag force to address the underprediction of the low-frequency surge force on the constrained platform.

We performed a sensitivity study to better understand the relation between the transverse drag coefficient and the low-frequency surge force. The transverse drag coefficient on the upper columns and the main column is altered, whereas that on the heave plate is kept constant at 1.6, as in Section 3.1, throughout the present investigation. Because of the exponentially decaying wave-field velocity with depth, the transverse drag on the heave plates has little contribution to the low-frequency surge force when the structure is fixed. The sensitivity study was done both with and without vertical wave stretching for the computation of the transverse drag force. The PSDs of surge force from this sensitivity study are shown in Fig. 5, and the corresponding PSD integrals are compared in Fig. 6.

As shown in Fig. 5a, the low-frequency surge force is relatively insensitive to the transverse drag coefficient on the upper columns and the main column without wave stretching. A very high drag coefficient of $C_D = 4$ is needed to obtain a low-frequency surge-force PSD integral comparable to that of the experiment (Fig. 6a). Further, the surge-force PSD from the OpenFAST simulation does not match the experimental measurements in the low-frequency range (Fig. 5a). Finally, the high C_D leads to an overprediction of the wave-frequency surge force (Fig. 6a) because of excessive viscous loads. All observations suggest that simply increasing the value of C_D is not the correct approach.

On the other hand, when vertical wave stretching is enabled, the low-frequency surge force becomes more sensitive to C_D . With $C_D = 1.6$, good agreement is observed between the experiment and the OpenFAST prediction both in terms of the low-frequency surge-force PSD (Fig. 5b) and PSD integral (Fig. 6b), lending confidence to the correctness of the model. The wave-frequency surge excitation

from the model remains in good agreement with the experiment as well. Furthermore, it can be concluded that the low-frequency surge force predominantly comes from the transverse drag force on the columns near the waterline in the periodically wetted zone, a third-order contribution, rather than from the submerged sections of the columns.

Whereas increasing C_D to 1.6 on the upper columns provides a good prediction of the low-frequency surge force with vertical wave stretching, it will result in incorrect surge free-decay behavior, which requires a drag coefficient of 0.4 [18]. We therefore propose the use of a depth-dependent transverse drag coefficient. For the permanently submerged portion of the columns (approximately defined as $z < -4$ m), the original value of $C_D = 0.4$ is used. The value of C_D is increased to 1.6 in the periodically wetted zone ($z > -3$ m) as shown in Fig. 7. With this approach, the OpenFAST model retains the correct behavior in surge free-decay and forced motion (see the NREL solutions in Ref. [9]) while predicting the correct low-frequency surge force when compared to the experiment.

The increased drag coefficient near the still water level is physically justifiable because the proximity to the free surface could lead to an increase in the effective sectional drag coefficient. This behavior has been observed with a vertical surface-piercing circular cylinder in a steady current [30] and, more recently, in regular waves [31]. This possible increase in the effective sectional drag coefficient warrants further detailed investigation that is beyond the scope of the present article.

With the depth-dependent transverse drag coefficient, the predicted wave force in surge is shown in Fig. 8 with comparison to the original OC6 OpenFAST model described in Section 3.1. A significantly improved prediction of the low-frequency surge force is achieved with the present model without affecting the wave-frequency surge force. Furthermore, the model also automatically generates greatly improved predictions of the floater surge motion under the freely floating condition (LC 5.3), lending more confidence to this modeling approach. The PSD and PSD integral of the surge motion are shown in Fig. 9. The agreement between the experiment and the present OpenFAST prediction is very encouraging. This comparison indicates that the underprediction of surge resonance motion previously observed [1,9] is primarily a consequence of underpredicting the low-frequency surge excitation rather than of overpredicting the surge damping. Note that if the additional global linear damping in surge of 75 kN s/m discussed in Section 3.1 is removed, the prediction of the low-frequency surge PSD integral by the present modified OpenFAST model will increase by approximately 21%, which corresponds to a 10% increase in the surge resonance amplitude. The added damping has a negligible

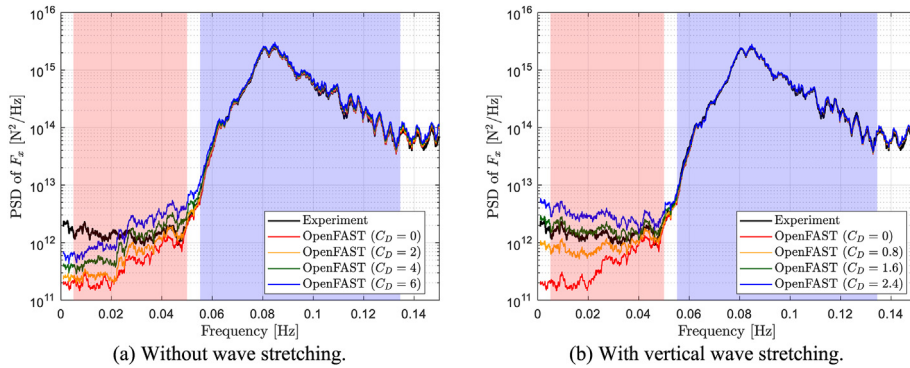


Fig. 5. Sensitivity of the surge force, F_x , on the fixed semisubmersible to the transverse drag coefficient, C_D , on the upper columns and the main column (a) without vertical wave stretching and (b) with vertical wave stretching. The structure is in the irregular waves of LC 3.3. The pink region indicates the low-frequency range, and the blue region is the wave-frequency range (see Table 2).

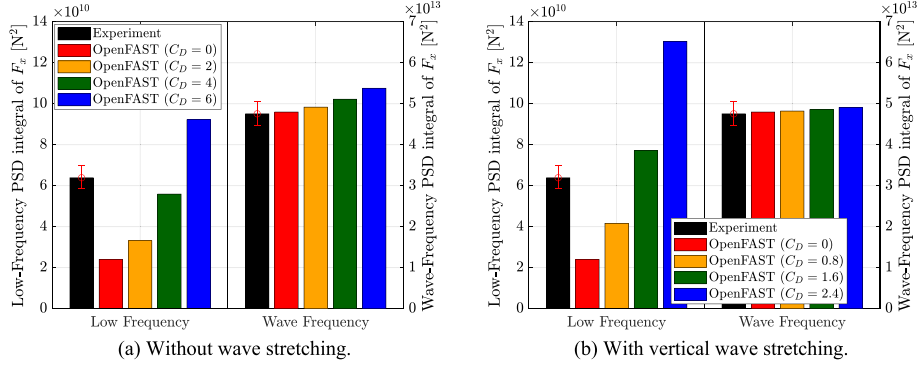


Fig. 6. Sensitivity of the PSD-integral metrics of the surge force, F_x , on the fixed semisubmersible to the transverse drag coefficient, C_D , on the upper columns and the main column (a) without vertical wave stretching and (b) with vertical wave stretching. The structure is in the irregular waves of LC 3.3.

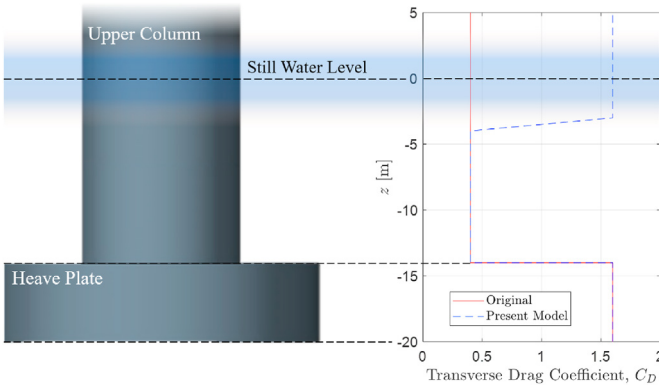


Fig. 7. Distribution of the transverse drag coefficient, C_D , along the upper column and heave plate. Compared to the original OC6 model [9,18], the present model uses depth-dependent C_D on the upper columns with increased drag coefficient in the periodically wetted zone (the blue shaded region).

effect on the wave-frequency surge response.

Taking a step further, the time histories of the surge motion from the experiment and model predictions are compared in Fig. 10. The phase of the low-frequency surge resonance motion is also consistent between the experiment and the present model. In comparison, the original model visibly underpredicts the low-frequency surge resonance.

The use of a depth-dependent transverse drag coefficient has a negligible effect on the model predictions in heave and pitch, which

means the increased drag coefficient near the waterline can be tuned independently to provide the correct level of low-frequency surge force and motion without any unexpected side effects. This greatly simplifies model tuning, which needs to be performed for different column cross-section geometries and, to a lesser extent, different wave conditions as demonstrated in Section 5.

The use of a depth-dependent transverse drag coefficient is not a new idea. This feature is readily available in the current version of OpenFAST and has been successfully applied to model the slow drift motion of floating offshore wind semisubmersibles in several prior investigations with a different floater geometry [15–17]; however, these prior studies directly tuned the drag coefficient against the experimental slow-drift motion without explicitly considering the low-frequency surge force on a fixed structure. In the present study, we have shown that the use of a depth-dependent drag coefficient can also lead to good agreement in the surge wave force on a fixed structure over the entire low-frequency region, and the same distribution of transverse drag coefficient automatically results in the correct low-frequency surge motion. This observation bolsters our confidence in the use of a depth-based drag coefficient.

4.2. Modification to the axial drag force on the heave plates

As shown in Fig. 4b, the underprediction of the low-frequency pitch moment on the fixed structure is not as severe when compared to the surge force. Most of the low-frequency pitch moment has already been captured by the second-order potential-flow QTF. The remaining difference between the experiment and the OpenFAST predictions is most likely a consequence of unsatisfactory modeling of the axial/normal drag force on the heave plates,

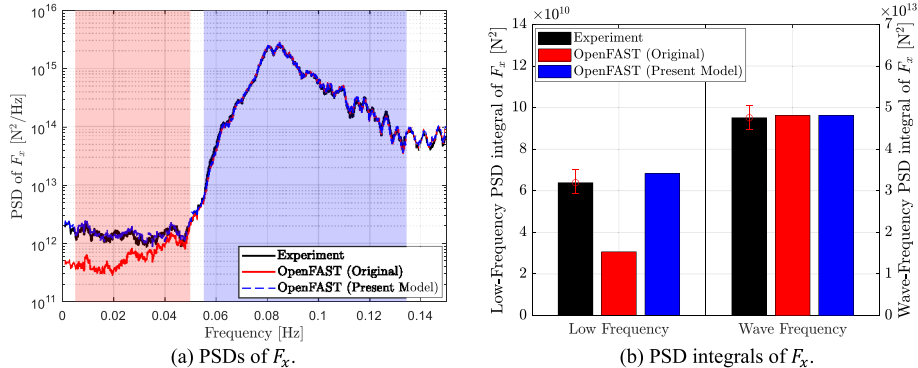


Fig. 8. Surge force, F_x , on the fixed semisubmersible in irregular waves (LC 3.3). (a) The PSDs of F_x are shown, with the pink region indicating the low-frequency range and the blue region indicating the wave-frequency range (see Table 2). (b) The PSD integrals of F_x are compared. The original OpenFAST model of [9] is described in Section 3.1. The present model utilizes the depth-dependent transverse drag coefficient.

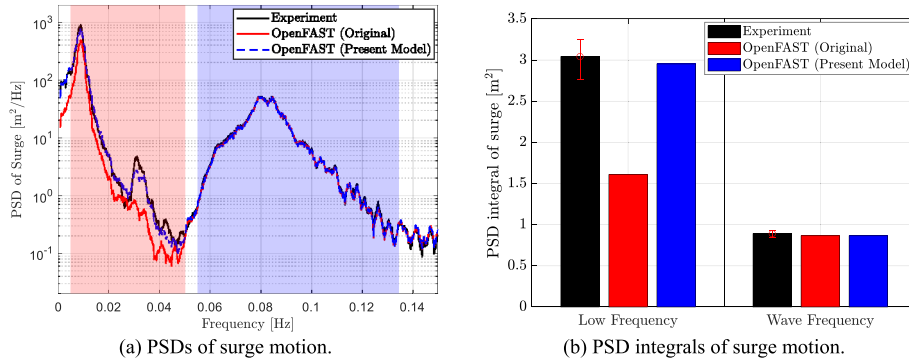


Fig. 9. Surge motion of the freely floating offshore wind semisubmersible in irregular waves (LC 5.3). (a) The PSDs of the surge motion are shown, with the pink region indicating the low-frequency range and the blue region indicating the wave-frequency range (see Table 2). In (b), the PSD integrals of the surge motion are compared. The original OpenFAST model of [9] is described in Section 3.1. The present model utilizes the depth-dependent transverse drag coefficient.

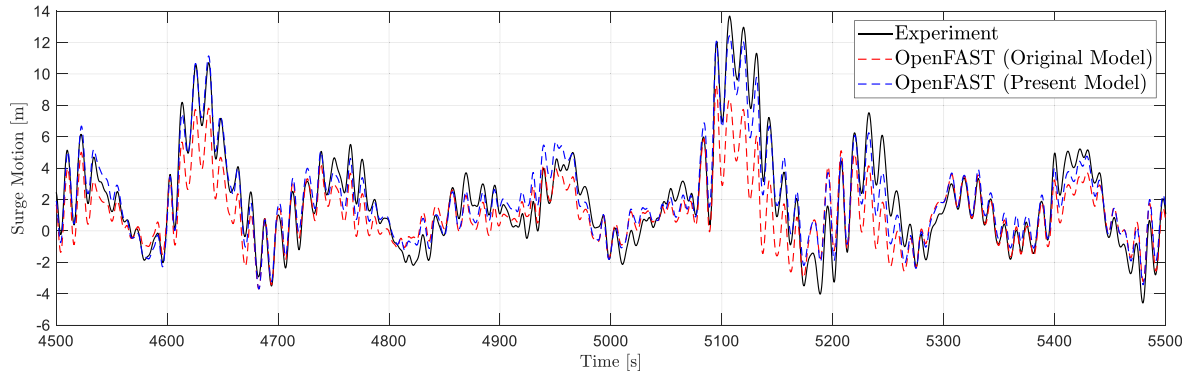


Fig. 10. Time series of the surge motion of the offshore wind semisubmersible in irregular waves (LC 5.3). The present model utilizes the depth-dependent transverse drag coefficient.

which is addressed in this section.

The sensitivity of the low-frequency pitch moment to the heave-plate axial drag coefficient $C_{D_{Ax}}$ is investigated in Fig. 11. The low-frequency pitch moment is not very sensitive to the axial drag coefficient as shown in Fig. 11a above 0.02 Hz, and the under-prediction persists even with a very high drag coefficient of 8, as indicated by the low-frequency pitch-moment PSD integral in Fig. 11b. With $C_{D_{Ax}} = 8$, the wave-frequency pitch moment is already significantly overpredicted. The heave force (not shown) also shows a very large error. This observation is consistent with that from Ref. [21], which states that the axial drag forces on the

heave plates primarily affect the pitch moment at the wave frequencies with only minor effects on the difference/low-frequency pitch moment. In fact, only the pitch moment near the very low surge natural frequency, 0.01 Hz, is weakly influenced by $C_{D_{Ax}}$, whereas the moment at the more relevant pitch natural frequency around 0.032 Hz is hardly affected at all. This behavior is also noted in Ref. [29]. This sensitivity study demonstrates that it is impossible to obtain satisfactory predictions of the pitch moment over both low frequencies and wave frequencies simultaneously by simply tuning the heave drag coefficient, $C_{D_{Ax}}$. Modifications to the existing formulation of the axial drag force were therefore investigated.

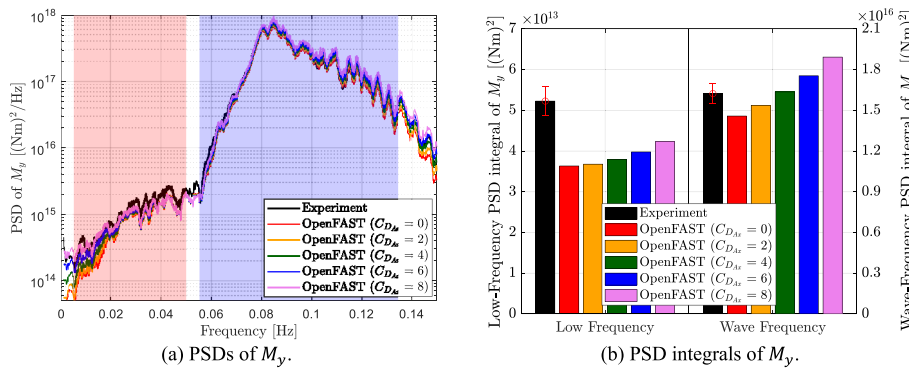


Fig. 11. Sensitivity of the (a) PSD and (b) PSD integrals of the pitch wave moment on the fixed offshore wind semisubmersible to the axial drag coefficient of the heave plates, $C_{D_{Ax}}$. The floater is in irregular wave (LC 3.3). In (a), the pink region indicates the low-frequency range, and the blue region is the wave-frequency range (see Table 2).

The existing axial-drag formulation used by OpenFAST is given in Section 3.1. One important feature is that the axial drag forces are evaluated and applied to both faces of the heave plates (top and bottom) as shown in Fig. 3, with half of the drag force on each face. This formulation is originally designed for Morison-equation-only members, meaning members not included in the potential-flow solution whose effects are only accounted for through the Morison equation. For such parts, this is an appropriate model. When the flow normal to the surface is directed toward the surface ($v_{r,n} < 0$), the force represents the effect of increased stagnation pressure on the surface. When the flow is directed away from the surface ($v_{r,n} > 0$), the force represents the low pressure on the surface caused by flow separation and a lack of pressure recovery; however, this formulation is not entirely appropriate for hybrid members, which are members already included in the potential-flow calculation with added empirical viscous drag forces. For such components, the contribution from the increased stagnation pressure on the face with $v_{r,n} < 0$ is already accounted for in the hydrodynamic coefficients from the potential-flow solution, which also has perfect pressure recovery on the opposite face with $v_{r,n} > 0$ because of a lack of viscous effects and flow separation; therefore, the additional axial viscous drag force for such parts should only approximate the difference between the potential-flow solution and the real viscous flow on the face with $v_{r,n} > 0$, caused by flow separation.

In other words, it is more appropriate to evaluate and apply the total axial drag force only on the face of the heave plates with $v_{r,n} > 0$ (i.e., the flow is directed away from the surface). Based on this argument, Eq. (2) is slightly modified:

$$\mathbf{F}_{D_{Ax}} = \frac{1}{2} C_{D_{Ax}} \rho \mathbf{A} |v_{r,n}| \max(v_{r,n}, 0). \quad (5)$$

Numerically, doubling the lead coefficient of $\frac{1}{4}$ in Eq. (2) to $\frac{1}{2}$ in Eq. (5) ensures that the modified formulation of Eq. (5) will provide the same drag force as the original Eq. (2) for a hypothetical uniform and constant flow normal to the heave plates with the same $C_{D_{Ax}}$, because we are only applying the force on the face with $v_{r,n} > 0$ instead of on both faces, top and bottom. Physically, doubling the drag force is also consistent with the fact that the perfect pressure recovery in the potential-flow solution on the face with $v_{r,n} > 0$ increases the discrepancy with the real viscous flow, which has a pressure drop from flow separation instead of an increase.

One interesting observation is that the effect of the proposed modification to the axial drag force diminishes with a decrease in the thickness of the heave plates. As the thickness of the heave plate

approaches zero, the modified axial drag force will reduce to the original formulation of Eq. (2); however, for the thick heave plates of the DeepCwind floater considered in the present study, the variation of the background incident wave-field velocity with depth is not negligible across the height of the heave plate, and the modified formulation of Eq. (5) results in small changes in the time history of the modeled heave-plate drag force.

In the present study, the large heave plates are included in the potential-flow computation; therefore, the axial drag force is calculated using Eq. (5) in the present modified model with the original axial drag coefficient of $C_{D_{Ax}} = 4.1$ from Section 3.1. The pitch excitation on the fixed structure (LC 3.3) as predicted by the present OpenFAST model is compared to the experimental measurements in Fig. 12. Interestingly, the proposed change to the axial drag closed the gap between the experimental and the model-predicted moment in the low-frequency region. The modification also has little effect on the wave-frequency moment, which is the desired behavior. To further illustrate the effect of Eq. (5) on the pitch moment, M_y , the PSDs of the contribution to M_y from the axial drag forces on the heave plates only are shown in Fig. 13. Comparing the results from Eq. (2) and Eq. (5), the largest relative increase in pitch moment obtained with Eq. (5) is between 0.01 Hz and 0.055 Hz, which exactly corresponds to the low-frequency range over which the nonlinear pitch moment is underpredicted by the original OpenFAST model, whereas the pitch moment in the wave-frequency range is hardly affected. To be exact, the use of Eq. (5) also slightly increases the pitch moment near the wave peak frequency of 0.083 Hz; however, the increase in pitch moment at the peak frequency is actually less than that in the low-frequency range near 0.047 Hz, which, coupled with the much higher level of pitch moment at the wave frequencies, results in negligible relative changes in the pitch moment. The fact that Eq. (5) leads to an increase in the nonlinear pitch moment over the correct frequency range lends further confidence to the proposed change to the axial drag force.

With the modified axial-drag formulation, the OpenFAST model is used to simulate the floater under a freely floating condition in irregular waves (LC 5.3). Compared to the original model, the predicted pitch resonance motion, shown in Fig. 14, is higher and agrees better with the experimental measurements because of the increased low-frequency pitch moment; however, the pitch motion is still underpredicted, suggesting that pitch damping is also overestimated at the pitch resonance frequency. This last issue is addressed in Section 4.3.

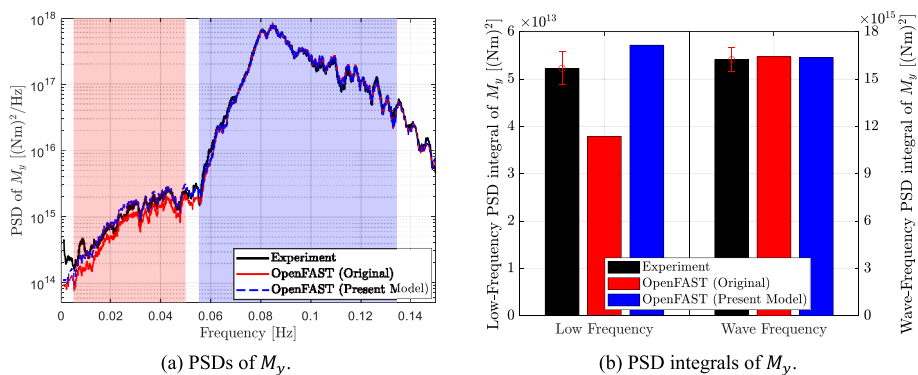


Fig. 12. Pitch moment, M_y , on the fixed offshore wind semisubmersible in irregular waves (LC 3.3). (a) The PSDs of M_y are shown, with the pink region indicating the low-frequency range and the blue region indicating the wave-frequency range (see Table 2). In (b), the PSD integrals of M_y are compared. The original OpenFAST model of [9] is described in Section 3.1. The present model is based on the modified axial drag of Eq. (5).

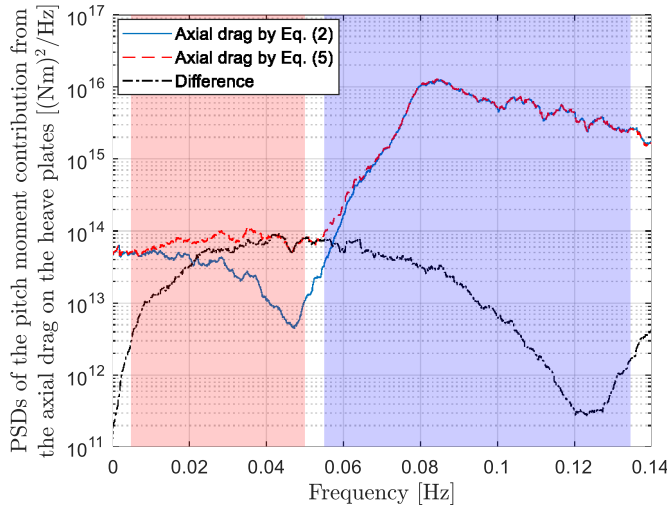


Fig. 13. Comparison of the PSDs of the pitch moment contributed by the axial drag force on the heave plates. The axial drag force is evaluated by the original OpenFAST formulation of Eq. (2) and the modified formulation of Eq. (5). The PSD of the difference between the results obtained using the two equations is also shown.

4.3. High-pass velocity filter for the drag force on the heave plates

To better understand the effects of the heave-plate axial drag coefficient, the freely floating structure in irregular waves (LC 5.3) was simulated with three different values of $C_{D_{Ax}}$ by the present OpenFAST model with the modified axial-drag formulation described in Section 4.2. The resulting heave and pitch motions of the floater are shown in Fig. 15. It is apparent that a low drag coefficient of $C_{D_{Ax}} = 1.6$ leads to better predictions of the pitch resonance motion at 0.032 Hz; however, the low drag coefficient leads to an overprediction of the heave resonance motion near 0.058 Hz. This is essentially the same issue encountered in Ref. [18], which suggested that the heave and pitch resonance motions require conflicting axial drag coefficients for the heave plates; however, this apparent conflict is likely not between the two modes of motion, rather it is the different frequency bands that require different drag coefficients. This is apparent from the results with the highest axial drag coefficient of $C_{D_{Ax}} = 7.2$, which show improved predictions of both the heave and pitch motions at the higher wave peak frequency of 0.083 Hz.

This observation shows that different axial-drag coefficients work better for different frequency ranges, with lower frequency

motion requiring a lower drag coefficient. This frequency dependence of the drag coefficient might be explained by the fact that the flow separation and alternate vortex shedding at the sharp corners of the heave plates are mostly controlled by the more rapid wave-frequency flow and body oscillation rather than by the slow body oscillation at the much lower pitch resonance frequency. It is therefore conceivable that the drag force would be more closely linked to the wave-frequency velocity components and react less strongly to the low-frequency velocity components, resulting in a higher effective drag coefficient for the former and a lower coefficient for the latter. This effect associated with the simultaneous presence of velocity components at multiple frequencies is likely distinct from the usual dependence of drag coefficient on the Keulegan-Carpenter (KC) number in harmonic flows. Furthermore, in a realistic, irregular-wave environment where the definition of the KC number is not straightforward, the KC-number effect is usually associated with the overall level of wave and structural motion amplitudes in the literature and tied to different sea states (see, e.g. Ref. [32]) rather than different frequency bands of a given sea state.

Whereas a frequency-dependent drag coefficient can be implemented in the frequency domain with linearized drag and an iterative solution, it is challenging to implement a proper frequency-dependent drag coefficient in a time-domain model like OpenFAST with quadratic drag forces. Boon [33] developed an alternative form of the Morison equation to include frequency-dependent drag coefficients for a fixed, surface-piercing vertical cylinder; however, it is difficult to apply to a floating structure when the relative flow velocity is not known a priori. Instead, we propose a simplified approach that approximates the required behavior of the heave-plate drag force to capture the low-frequency pitch resonance motion without adversely affecting the prediction of the heave resonance motion. This is achieved with the help of a simple first-order high-pass filter for the relative normal velocity $v_{r,n}$ in Eq. (5). Higher-order passive filters are not recommended because of the excessive phase shift. The filter equation in discrete time is given by

$$\tilde{v}_{r,n}^i = C\tilde{v}_{r,n}^{i-1} + C(v_{r,n}^i - v_{r,n}^{i-1}), \quad (6)$$

where i is the time-step number and $\tilde{v}_{r,n}^i$ is the filtered relative normal velocity. The filter coefficient, C , is given by

$$C = \exp(-2\pi f_c / f_s), \quad (7)$$

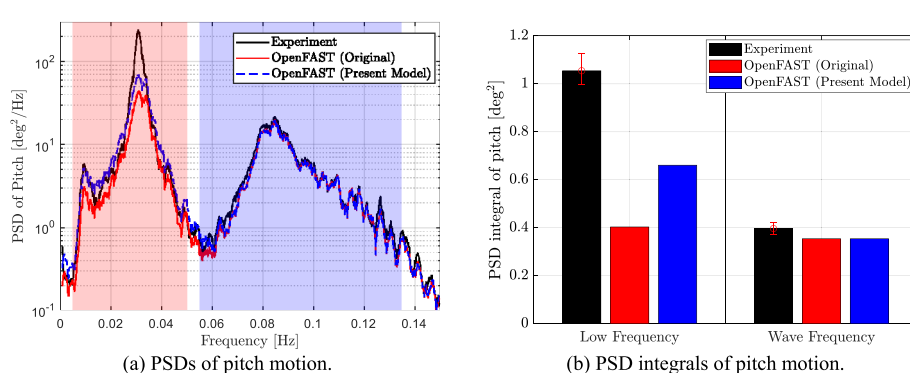
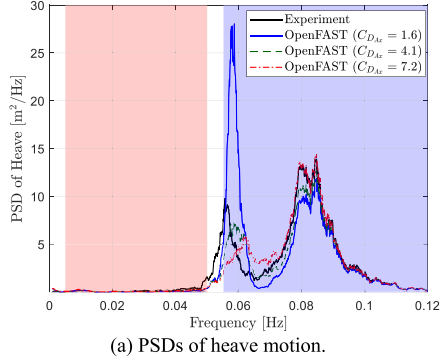
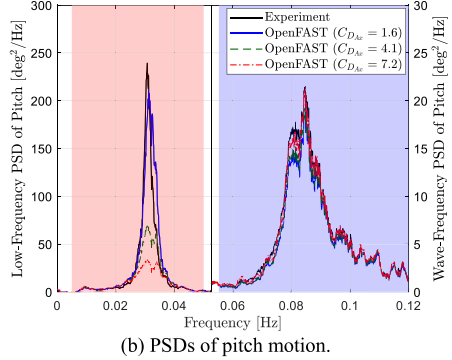


Fig. 14. Pitch motion of the freely floating offshore wind semisubmersible in irregular waves (LC 5.3). (a) The PSDs of the pitch motion are shown, with the pink region indicating the low-frequency range and the blue region indicating the wave-frequency range (see Table 2). In (b), the PSD integrals of the pitch motion are compared. The original OpenFAST model of [9] is described in Section 3.1. The present model is based on the modified axial drag of Eq. (5).



(a) PSDs of heave motion.



(b) PSDs of pitch motion.

Fig. 15. PSDs of (a) heave motion and (b) pitch motion of the freely floating offshore wind semisubmersible in irregular waves (LC 5.3) with different axial drag coefficients, $C_{D_{Ax}}$. The axial drag was computed using Eq. (5). Note that in (b), two different scales are used for the low- and wave-frequency ranges.

where f_c and f_s are the cutoff frequency and sampling frequency (inverse of time step), respectively.

Note that it is important to filter the relative velocity rather than the drag force itself. The latter approach will also remove the low-frequency viscous moment in pitch on a fixed structure. The former will leave the low-frequency pitch moment shown in Section 4.2 mostly unaffected because the low-frequency viscous excitation primarily comes from the quadratic interaction of the wave-frequency velocity components that are weakly affected by the high-pass filter. Only the drag force induced by the low-frequency velocity component is reduced, following the rationale that the flow separation and vortex shedding at the corners of the heave plates and, by extension, the heave-plate drag force responds more strongly to the wave-frequency flow velocity and body oscillation. With the filtered relative velocity, $\tilde{v}_{r,n}$, the axial drag force is given by

$$\mathbf{F}_{D_{Ax}} = \alpha \mathbf{F}_{D_{Ax},0} + (1 - \alpha) \mathbf{F}_{D_{Ax},f}, \quad (8)$$

where

$$\mathbf{F}_{D_{Ax},0} = \frac{1}{2} C_{D_{Ax}} \rho \mathbf{A} |\tilde{v}_{r,n}| \max(\tilde{v}_{r,n}, 0) \quad (9)$$

and

$$\mathbf{F}_{D_{Ax},f} = \frac{1}{2} C_{D_{Ax}} \rho \mathbf{A} |\tilde{v}_{r,n}| \max(\tilde{v}_{r,n}, 0). \quad (10)$$

The scaling factor, $\alpha \in [0, 1]$, controls the reduction in effective axial drag coefficient for the low-frequency velocity components.

With the introduction of the high-pass filter, two additional tunable model parameters are introduced: the cutoff frequency, f_c , and the scaling factor, α , for the axial drag coefficient. In the present investigation, f_c is always set to 0.07 Hz, just below the wave peak frequency of 0.083 Hz. The scaling factor α was set to 0.5 as an initial guess, which produced good predictions; therefore, no further tuning was performed. The axial drag coefficient, $C_{D_{Ax}}$, was kept as 4.1 as in the original model in Section 3.1. One drawback of the current approach is that, strictly speaking, some a priori knowledge of the motion response of the structure from either wave-basin experiments or CFD simulations is required to tune the scaling factor, α .

With this final modification to the OpenFAST model, the PSDs of the predicted heave and pitch motions of the structure in irregular waves (LC 5.3) are shown in Fig. 16. The experimental measurements and the predictions by the original model of Robertson et al. [9] are both included for reference. The corresponding PSD integrals are shown in Fig. 17. The addition of the high-pass filter

leads to good agreement between the present modified OpenFAST model and the experiment for both the heave resonance motion and the low-frequency pitch resonance motion (for comparison, see Fig. 14 for the results without the high-pass filter). Note that without the additional global linear damping in pitch of 31 MN·m s/rad discussed in Section 3.1, the prediction of the low-frequency pitch PSD integral by the present modified OpenFAST model will increase slightly by approximately 8%, which corresponds to a 4% increase in the pitch resonance amplitude. The added damping has a negligible effect on the wave-frequency pitch response.

The heave resonance peak frequency is slightly shifted in the model prediction compared to the experiment because the actual heave added mass is slightly higher than the linear potential-flow prediction owing to viscous effects (recently confirmed for this exact floater geometry using CFD simulations [34]). This effect tends to be more significant for flat-bottomed bodies [35] and can be corrected by simply applying a scaling factor for the potential-flow added mass [36], which was not done for the present results. The floater motion near the wave peak frequency of 0.083 Hz remains unaffected. It is possible that a more sophisticated filter design can lead to further improved agreement between the model and the experiment across all frequency ranges; however, the current simple filter is considered adequate while having the benefit of keeping the number of tunable parameters to a minimum.

Note that the addition of the filter has practically no effect on the wave excitation in surge on the structure under a fixed condition or on the prediction of surge motion; both remain in good agreement with the experiment as shown in Section 4.1. The effects of using the filtered velocity on the pitch moment on the structure under the fixed condition are illustrated in Fig. 18. The PSDs of the pitch moment obtained with Eq. (5) and Eq. (8) are very similar, as shown in Fig. 18a; using the filtered velocity slightly reduces the low-frequency PSD integral of the pitch moment (Fig. 18b), resulting in slightly improved agreement with the experiment given the same value of $C_{D_{Ax}}$ of 4.1.

The comparison of heave force on the fixed structure is shown in Fig. 19. Overall, the modified model with Eq. (8) for heave-plate drag produces improved predictions of the low-frequency heave force above 0.02 Hz and of the wave-frequency force below 0.07 Hz (see Fig. 19a); however, a slight overprediction near the surge resonance frequency of 0.01 Hz is also observed with both Eq. (5) and Eq. (8). The use of the filtered velocity in Eq. (8) alleviates this overprediction, resulting in better agreement with the experiment in terms of the low-frequency PSD integral of the heave force compared to using Eq. (5). Either way, the low-frequency heave excitation is of little engineering importance because the heave

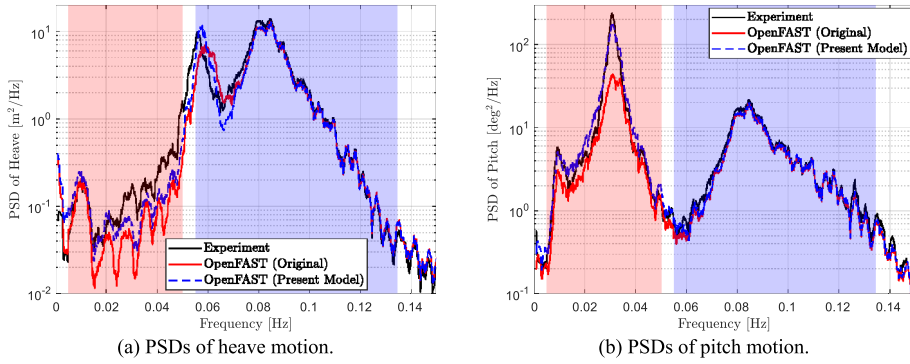


Fig. 16. PSDs of (a) heave motion and (b) pitch motion of the freely floating offshore wind semisubmersible in irregular waves (LC 5.3). With the present model, the axial drag was computed using Eq. (8). The pink region indicates the low-frequency range, and the blue region is the wave-frequency range (see Table 2). For comparison, the pitch motion predicted without the filtered velocity using Eq. (5) is shown in Fig. 14.

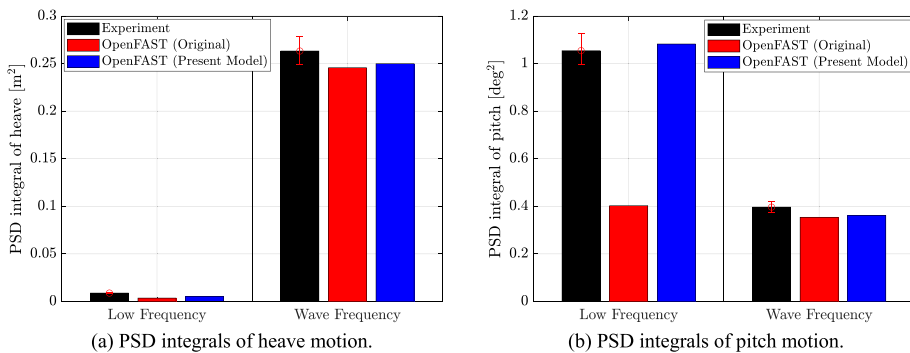


Fig. 17. PSD integrals of (a) heave motion and (b) pitch motion of the freely floating offshore wind semisubmersible in irregular waves (LC 5.3). With the present model, the axial drag was computed using Eq. (8).

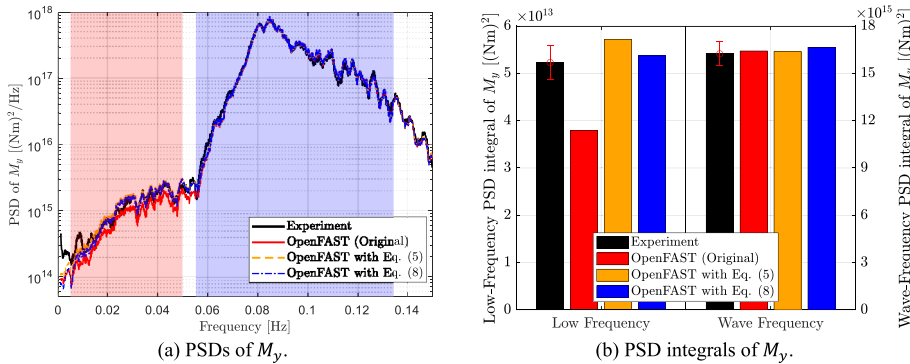


Fig. 18. Comparisons of (a) PSD and (b) PSD integrals of the pitch moment on the fixed offshore wind semisubmersible in irregular waves (LC 3.3) predicted using Eq. (5) (without filtered velocity) and Eq. (8) (with filtered velocity) for the axial heave-plate drag force. The pink region indicates the low-frequency range, and the blue region is the wave-frequency range (see Table 2). The original OpenFAST model of [9] is described in Section 3.1.

resonance frequency of this structure is much higher at around 0.58 Hz and is excited by the stronger direct wave-frequency excitation. All OpenFAST models predict approximately the same wave-frequency heave excitation.

Finally, we emphasize that the robust modeling of drag force in complex flow environments remains an open question. Although we have strived to provide physical justifications of using a high-pass-filtered relative velocity in the computation of heave-plate drag force, the proposed model is still a heavily simplified and approximate one based more on empirical observation of the

experimental measurements. The model obviously does not capture the highly complex flow behavior near the corners of the heave plates; however, at the same time, it is apparent that the proposed drag formulation improved the model predictions of not just the pitch motion under a floating condition but also the heave force on the fixed structure for the wave conditions investigated in this article with no detrimental side effects on the prediction of other metrics (also, see Section 5). Further investigation is needed to better establish the validity and the range of applicability of the proposed formulation with the filtered velocity.

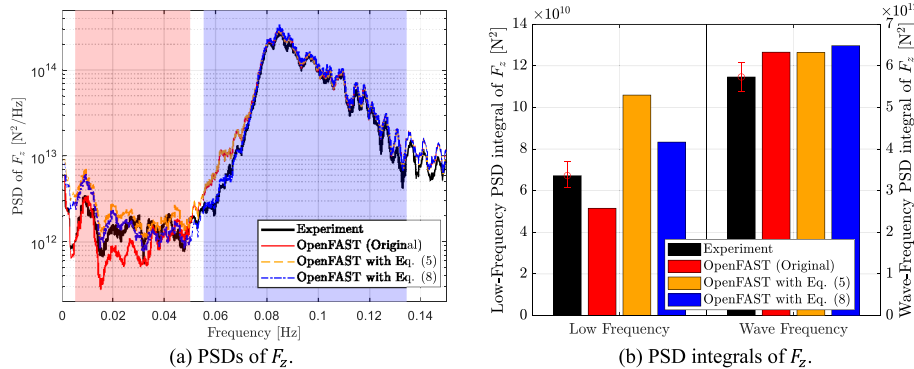


Fig. 19. Comparisons of (a) PSD and (b) PSD integrals of the heave force on the fixed offshore wind semisubmersible in irregular waves (LC 3.3) predicted using Eq. (5) (without filtered velocity) and Eq. (8) (with filtered velocity) for the axial heave-plate drag force. The pink region indicates the low-frequency range, and the blue region is the wave-frequency range (see Table 2). The original OpenFAST model of [9] is described in Section 3.1.

4.4. Summary of all modifications to the OpenFAST model

All modifications to the OpenFAST model described in Section 4 are made with respect to the drag force, both transverse and axial. The changes and the model coefficients used are summarized in Table 3. Overall, the present model has succeeded, at least for the load cases considered, in the task of accurately capturing the surge and pitch resonance excited by the nonlinear, low-frequency wave excitation. As discussed previously, this is a nontrivial task as indicated by the recent studies of Robertson et al. [1,9], which showed that most state-of-the-art engineering models for floating offshore wind turbines severely underestimate both low-frequency excitation on a fixed platform and the corresponding motion response of a floating platform. Furthermore, the current approach reconciles the fixed condition and the floating condition by obtaining good predictions for both using a single unified model with the same set of coefficients.

5. Blind validation of the modified model with white-noise waves

Using the modified OpenFAST model, the hydrodynamic forces on the OC6-DeepCwind semisubmersible when fixed and the motion response while freely floating in the white-noise waves (LC 3.4 and LC 5.4, respectively, in Table 2) were also computed as an additional blind validation. Although we had access to the experimental results for the white-noise waves beforehand, these data were not referenced when tuning the model parameters.

The wave loads on the fixed semisubmersible are shown in Fig. 20 (LC 3.4). Compared to the original model, the present modified model predicts higher low-frequency surge force because of the increased drag coefficient near the waterline. As shown in

Fig. 20a, the low-frequency surge force from the present model appears to be more consistent with the experiment; however, the PSD integrals shown in Fig. 20d suggest the present model over-predicts the low-frequency surge excitation, whereas the original model underpredicts. It is likely that much better agreement with the experiment in the low-frequency surge excitation can be achieved with the present model by slightly reducing the transverse drag coefficient near the waterline; however, this was not done, in the spirit of blind validation.

In Fig. 20b and 20e, both OpenFAST models produce similar predictions for the heave force, with the present model showing slightly better agreement with the experiment over the wave-frequency range. The present model also provides an improved prediction of the low-frequency pitch moment compared to the original model with the modified formulation of the heave-plate axial drag force of Eq. (8).

The motion of the semisubmersible when freely floating in white-noise waves (LC 5.4) is shown in Fig. 21. The low-frequency surge resonance motion is slightly overpredicted by the present model as shown in Fig. 21d, whereas the original model shows better agreement with the experiment. This is likely caused by the overprediction of the low-frequency surge force shown in Fig. 20a and 20d. The two OpenFAST models both show reasonably good agreement with the experiment in terms of the wave-frequency heave-motion PSD integral in Fig. 21e, with one underpredicting and the other slightly overpredicting. The most significant improvement with the present model is in the prediction of the low-frequency pitch resonance motion shown in Fig. 21c and 21f. The pitch resonance is severely underpredicted by the original model, whereas the present model shows very good agreement with the experiment in terms of the low-frequency pitch-motion PSD integral.

Table 3

Summary of the proposed modifications to the OpenFAST model for improved low-frequency predictions.

	Original OC6 Model	Present Modified Model	Effects
Transverse drag	Uniform $C_D = 0.4$ on the upper columns and the main column.	$C_D = 1.6$ near the waterline. $C_D = 0.4$ on the submerged section of the upper columns and the main column.	Improves the prediction of low-frequency surge force on the fixed structure and surge motion of the floating structure.
Heave-plate axial/normal drag	Axial drag force evaluated and applied at both faces (top and bottom) of the heave plates. Eq. (2) with $C_{D_{Ax}} = 4.1$.	Axial drag force only evaluated and applied at the face with $v_{r,n} > 0$, meaning the normal flow points away from the heave plate. Part of the drag computed from high-pass-filtered relative normal flow velocity. Eq. (8) with $C_{D_{Ax}} = 4.1$.	Evaluating the axial drag force only on the face with $v_{r,n} > 0$ improves the prediction of low-frequency pitch moment on a fixed structure. Computing part of the drag force using high-pass-filtered relative normal flow velocity improves the prediction of low-frequency pitch resonance.

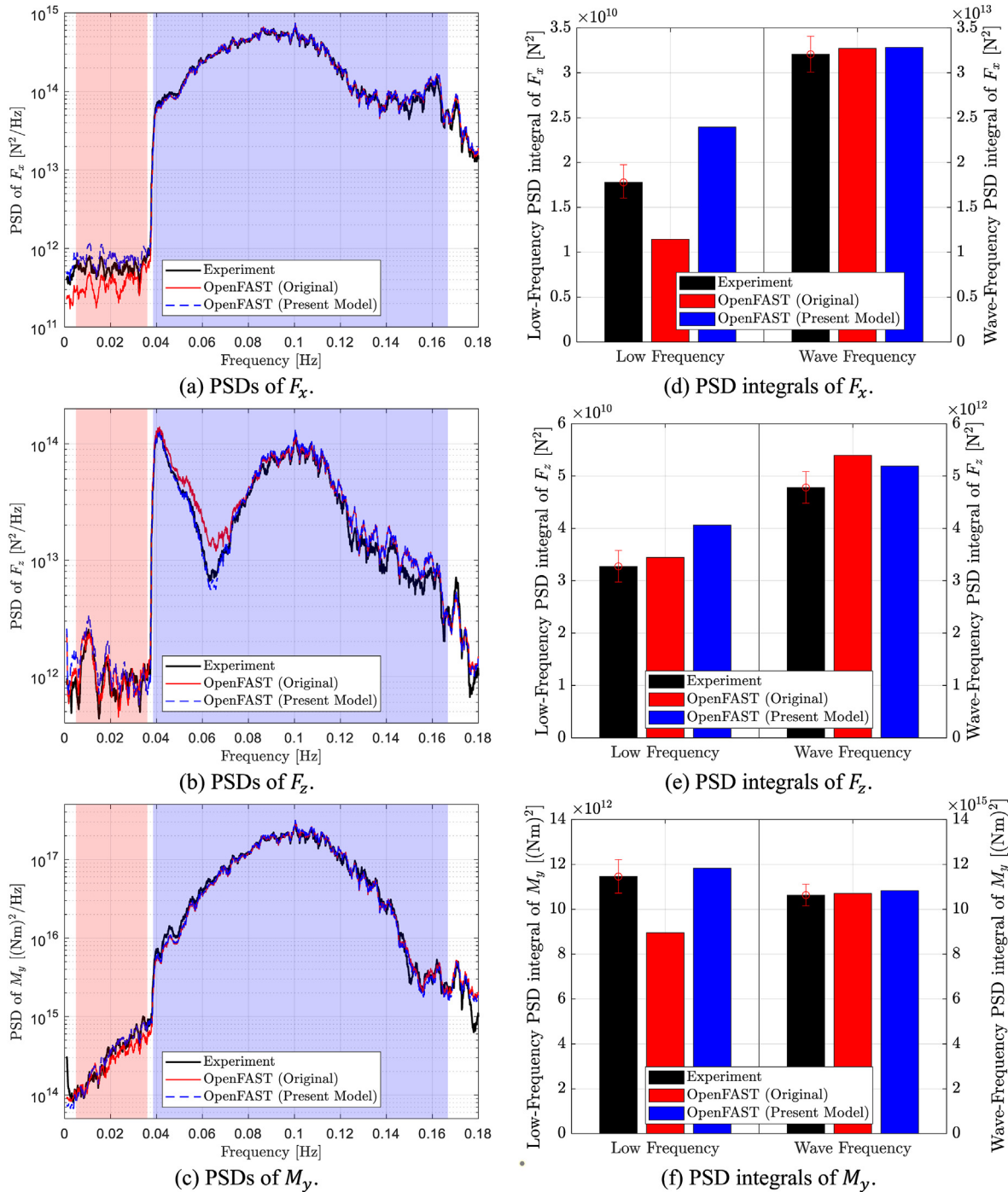


Fig. 20. PSDs of wave-induced (a) surge force, (b) heave force, and (c) pitch moment on the fixed offshore wind semisubmersible in the white-noise waves (LC 3.4), and (d–f) the corresponding PSD integrals. In (a–c), the pink region indicates the low-frequency range, and the blue region is the wave-frequency range (see Table 2).

Overall, the present modified model gives reasonable predictions, for the white-noise waves, of both the wave excitation on the fixed structure and the motion of the floating structure in both low-frequency and wave-frequency ranges without any retuning. This suggests that the modified model is reasonably general with regard to the input waves and should provide adequate predictions for a range of wave conditions. This is, of course, a highly valuable feature in engineering models for design purposes. With the white-noise waves, the most significant improvements compared to the

original model are in the low-frequency pitch moment and pitch motion, whereas the improvements to low-frequency surge force and motion are not as obvious as with the irregular-wave condition of LC 3.3 and LC 5.3; however, it should be emphasized that the wide-band white-noise sea state is rather unrealistic, and we believe that with a minimal amount of tuning, the present model can still provide improved predictions in surge when dealing with more realistic narrow-banded sea states, as demonstrated with LC 3.3 and LC 5.3 in Section 4.

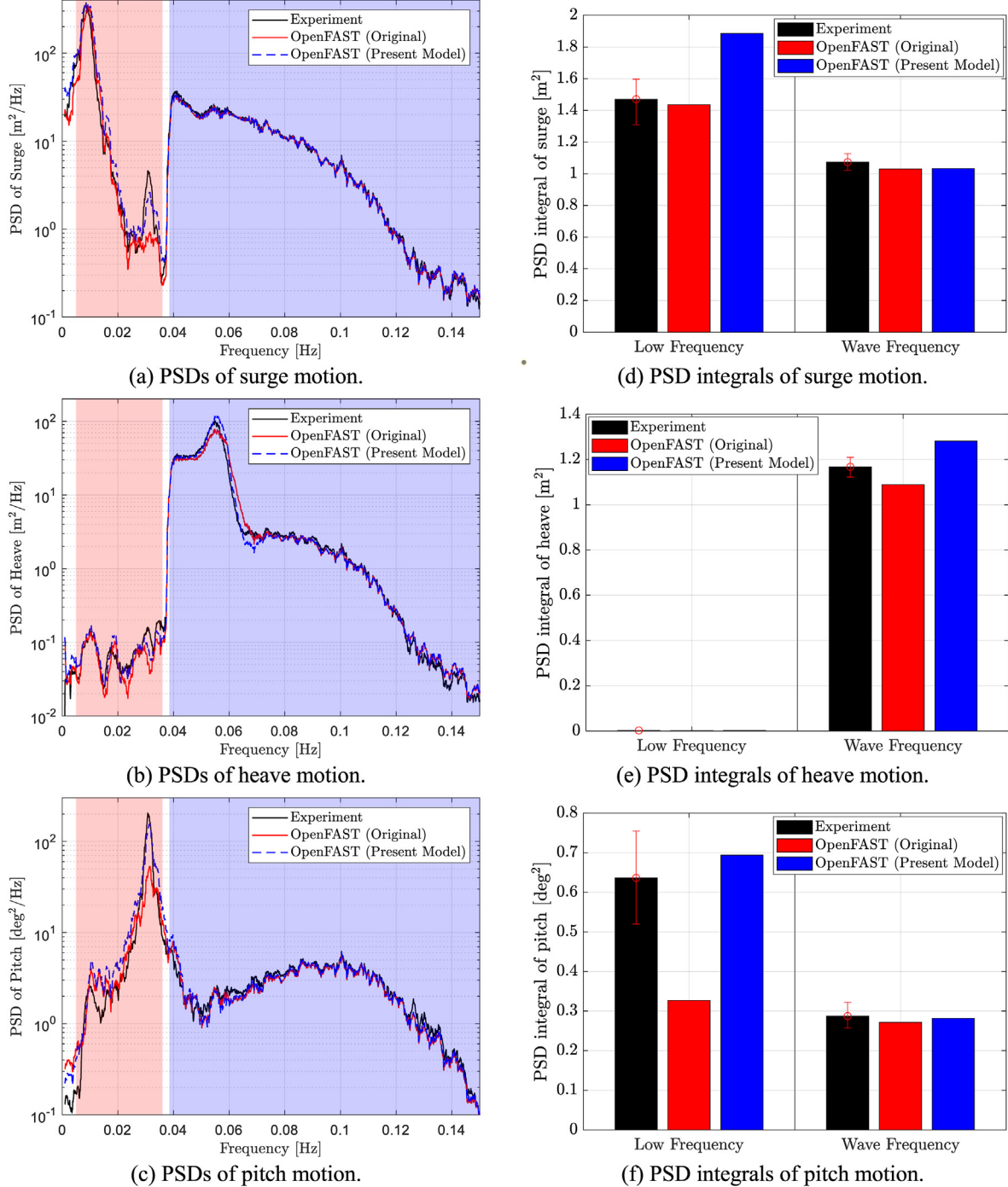


Fig. 21. PSDs of wave-excited (a) surge motion, (b) heave motion, and (c) pitch motion of the freely floating offshore wind semisubmersible in the white-noise waves (LC 5.4), and (d–f) the corresponding PSD integrals. In (a–c), the pink region indicates the low-frequency range, and the blue region is the wave-frequency range (see Table 2).

6. Discussions and recommendations for future applications

Similar to the QTF-correction method of Li and Bachynski-Polić [21], the modifications to the empirical drag forces presented in the current article are aimed at providing candidate solutions to the underprediction of the low-frequency wave excitation and responses of floating wind semisubmersibles by mid-fidelity engineering models [1,9], a common issue encountered not just with the DeepCwind semisubmersible investigated here but also with many other floater designs (e.g. Refs. [2,3,15]); however, the philosophies

behind the present approach and that of [21] are very different.

The method of correcting the QTFs from second-order potential-flow theory is based on leveraging the CFD solutions as much as possible in a quantified fashion. The results from many CFD simulations spanning a range of frequencies are used to modify the QTFs; therefore, it can be expected that this method will yield accurate predictions of the nonlinear, difference-frequency wave loads for a wide range of wave frequencies, at least for a fixed structure and when the wave amplitudes are similar to those used in the CFD simulations. This method is more numerical in nature.

In the present work, we attempted to identify the underlying physical mechanisms that are missing in the mid-fidelity models that are causing the underprediction, and we proposed modifications to the empirical drag forces based on general physical arguments aimed at addressing the identified deficiencies. We also strived to make the modifications as simple as possible and introduce minimal additional tunable parameters. It is our hope that the proposed solution can be more easily applied in practice.

The QTF-correction method [21] was demonstrated to be highly effective in improving the low-frequency predictions; however, there remain some open questions and limitations, which we hope to circumvent with the alternative approach proposed in this article.

First, a proper application of the QTF-correction method requires many bichromatic-wave CFD simulations, which need to be repeated whenever the design changes. To some extent, this requirement negates the advantage of mid-fidelity models in design optimization. The correction of the QTFs (both magnitude and phase), which depends on two frequencies, is also not trivial. In Ref. [21], the possible frequency pairs over the frequency range of interest were mapped into different regions, and, over each region, different assumptions were made about the corrected QTF values to facilitate the correction based on the available CFD results. It is unclear whether the proposed mapping and the associated assumptions about the QTFs are generally applicable to different floater geometries. The alternative method documented in the present article, on the other hand, does not require as many CFD simulations to tune the few additional model parameters. Of course, some *a priori* information is still required to tune the model as with any mid-fidelity approach. For instance, the nonlinear, low-frequency surge force is primarily controlled by just one parameter, the increased drag coefficient near the waterline, which can be determined from just a few sets of CFD simulations or experimental measurements. The modification to the axial drag force on the heave plates that improves the low-frequency pitch moment introduces no new parameters that require tuning. The drawback of the present method compared to the QTF-correction approach is that the range of frequencies over which the predictions of the nonlinear, low-frequency wave loads remain accurate is not as obvious.

Second, the nonlinear, low-frequency excitation might not always be quadratic in nature. For instance, the present work suggests that the viscous drag force near the waterline, in conjunction with wave stretching, is the dominant contributor to the low-frequency surge excitation. This is a third-order effect; therefore, the method of modifying the QTFs might lead to errors when the wave amplitudes are different from those used in the CFD simulations, because this method forces the correction to the low-frequency excitation to scale quadratically with wave amplitude. In the present work, we hope that by identifying the underlying physical cause of the underprediction, the results will scale more appropriately with the incident wave amplitudes, at least within a moderate range.

Finally, application of the QTF-correction method to a floating structure requires the assumption that the same corrections to the QTFs determined from the CFD simulations of a restrained structure in bichromatic waves (i.e., the differences between the QTFs for a fixed structure estimated from the CFD simulations and from the second-order potential-flow theory) remain valid and can be used to directly modify the QTFs of a floating structure from potential-flow theory [22]. This assumption requires further investigation, especially when viscous drag plays a major role in the nonlinear low-frequency excitation. In contrast, the modifications to the Morison drag forces proposed in the present work should be equally applicable to a fixed structure and a moving structure when the relative flow velocity is used.

Overall, both the present approach and the QTF-correction method [21] provide significantly improved predictions of the low-frequency wave excitation and responses of a floating wind semisubmersible for the wave conditions and floater geometry investigated. At the same time, both leave some open questions as to their applicability to changes in wave conditions and floater geometries. The modeling techniques proposed in this article, developed based on a different philosophy, represent a possible alternative to the QTF-correction method [21].

Although the underprediction of the low-frequency resonance responses of floating wind semisubmersibles is a common issue, the modifications to the OpenFAST model presented in this article are specifically devised with the OC6-DeepCwind semisubmersible in mind, for which we have limited but high-quality experimental measurements. Without access to good-quality experimental data for other floater designs, it is difficult to draw any definitive conclusion on the applicability of the proposed changes to the OpenFAST model to other floater geometries. Nevertheless, based on the physical arguments behind the modifications, we conjecture the following guidance for future applications to other floater designs:

- 1) We believe an increased transverse drag coefficient near the waterline (discussed in Section 4.1) should be used for vertical surface-piercing circular columns whenever low-frequency surge resonance is of concern. The increase in effective drag coefficient near the waterline has been observed in prior studies for a single circular cylinder in isolation in both current [30] and wave conditions [31] and is likely a common phenomenon; however, the drag coefficient near the waterline will likely have to be tuned to some degree if vastly different wave conditions are considered. The use of increased waterline drag coefficients for surface-piercing columns of different cross sections, such as a square column, requires further investigation. In this case, the drag coefficient will also strongly depend on the wave direction, which is not considered in the present investigation.
- 2) As discussed in Section 4.2, the modification to the axial drag coefficient on the heave plates, which limits the drag force to the face with $v_{r,n} > 0$ (normal flow velocity pointing away from the face) is only required when the floater design incorporates thick heave plates like the DeepCwind semisubmersible. If the low-frequency pitch moment is underpredicted, this modification will likely improve the results. For thin heave plates, this modification will not have a significant impact; however, if the diameter of the heave plate relative to the diameter of the upper column is close to unity, the modified formulation of Eq. (5) can still be used to prescribe different drag coefficients depending on the flow direction to reflect the asymmetry about the heave-plate plane. This is not explored in the present study because of the large heave-plate diameter relative to the column diameter (see Section 4.2).
- 3) The high-pass filtering of the normal relative flow velocity when computing the heave-plate drag force discussed in Section 4.3 is also based on the general physical argument that the vortex shedding at the corners of the heave plates is mostly controlled by the more rapid wave-frequency flow and body oscillation rather than the body motion at the low pitch resonance frequency. As a result, the drag force would be more closely linked to the wave-frequency velocity components and would react less to the low-frequency velocity components. We believe this velocity filtering is generally applicable to semisubmersible designs with heave plates and with a pitch resonance frequency below the wave-frequency range; however, the filter parameters will require some tuning based on the specific floater design and the incident wave peak frequency.

Inevitably, mid-fidelity hydrodynamic modeling based on potential-flow theory and empirical drag forces needs to be tailored and tuned to some degree to the specific floater design and wave conditions being analyzed. Rather than developing a model that works for all semisubmersible designs and wave conditions automatically, which is not possible in our opinion, the intention of the present work is to suggest several simple yet physically justifiable modifications to the hydrodynamic modeling of offshore wind semisubmersibles that could potentially lead to significant improvements in the model predictions should future modelers also encounter difficulties with the low-frequency nonlinear load and responses. If and which modifications are needed should be decided at the discretion of future modelers depending on the specific floater design and wave conditions.

7. Conclusions

In the previous OC5 project and the ongoing OC6 project, the state-of-the-art, mid-fidelity engineering-level tools for floating offshore wind turbines were found to consistently underpredict the low-frequency responses of semisubmersible offshore wind platforms, both loads and motion. To address this deficiency, a modified OpenFAST model was developed in the present article as a major outcome of the OC6 Phase I investigation, which involved a three-way validation study with mid-fidelity engineering-level tools, high-fidelity CFD simulations, and wave-basin experiments into the low-frequency responses of offshore wind semisubmersibles.

Throughout this study, the open-source OC6-DeepCwind semisubmersible offshore wind platform was adopted as a generic design. Four load cases from the OC6 Phase I investigation were used: 3.3, 3.4, 5.3, and 5.4. LC 3.3 and LC 5.3 have the same JONSWAP incident wave spectrum, with LC 3.3 having a fixed platform and LC 5.3 a freely floating platform. LC 3.4 and LC 5.4 both have the same white-noise incident waves, with LC 3.4 corresponding to a fixed condition and LC 5.4 a freely floating condition. Experimental measurements for all four load cases are available from the OC6 Phase I experimental validation campaign. The experimentally measured wave forces and moments from LC 3.3 and the floater pitch motion from LC 5.3 were used to tune the modified OpenFAST model; the measured forces and moments from LC 3.4 as well as the measured motion responses from LC 5.4 were reserved for a blind validation and were not referenced during model tuning.

Based on the data gathered from the OC6 Phase I project, we proposed three changes to the OpenFAST model formulation and modeling practice that improve the predictions of the low-frequency responses without significantly increasing the difficulty of model parameter tuning. The number of tunable model parameters was deliberately kept low to avoid overfitting.

First, we identified the transverse viscous drag force on the vertical columns near the waterline to be the primary contributor to the nonlinear, low-frequency surge force near the very low surge resonance frequency. In contrast, second-order wave diffraction has a negligible contribution in this frequency range. This is consistent with the observation made during the CFD investigation of OC6 Phase I. We therefore proposed the use of an increased transverse drag coefficient in the region near the free surface in conjunction with vertical wave stretching. At the same time, to avoid excessive surge damping under a freely floating condition, a lower transverse drag coefficient previously tuned against free-decay and forced-oscillation experiments was used for the submerged section of the columns. This use of a depth-dependent drag coefficient led to excellent agreement with the experiment in the wave surge force throughout the entire low-frequency range for LC 3.3 and in the low-frequency surge resonance motion for LC 5.3.

Second, we modified the formulation of the axial/normal viscous drag on the faces of the heave plates. In the original model, the axial drag force is simultaneously applied to the face toward and away from the flow. Whereas this is an appropriate formulation for bodies that are modeled with the Morison equation only, it is not entirely suitable for members already modeled by potential flow, like the heave plates, because the increased pressure on the face toward which the flow is directed is already accounted for in the potential-flow solution. We therefore modified the OpenFAST model to only evaluate and apply the axial drag force on the face from which the flow is directed away to account for the effect of flow separation. Although this modification has negligible effects for thin heave plates, the OC6-DeepCwind floater incorporates thick heave plates with nonnegligible variation of the incident wave-field velocity with depth across the height of the heave plates; this modification led to much better agreement with the experiment in the low-frequency pitch moment on the fixed platform for both LC 3.3 and LC 3.4.

Finally, by inspecting the effects of the axial drag coefficient for the heave plates on the heave and pitch motion of the structure, it was observed that a lower drag coefficient improved the agreement between the model prediction and the experiment in the low-frequency range near pitch resonance, whereas an increased drag coefficient improved the agreement at higher frequencies. It is, however, difficult to implement frequency-dependent drag coefficients in a time-domain model like OpenFAST; therefore, a simplified approach was proposed in which part of the axial drag force is calculated based on a high-pass-filtered relative normal flow velocity. This modification led to good agreement between the model and the experiment in both the low-frequency pitch resonance motion and the wave-frequency heave resonance motion for both LC 5.3 and LC 5.4.

Overall, the new unified model with a single set of coefficients presented in this article simultaneously provides good predictions of the nonlinear, low-frequency excitation on a fixed offshore wind semisubmersible and the resonance motions in surge and pitch of the same structure when freely floating. For LC 3.3, the nonlinear, low-frequency wave surge force and pitch moment on the fixed structure predicted by the new modified OpenFAST model are within a 7% and 3% difference from the experimental measurements, respectively, in terms of the low-frequency PSD integrals. In comparison, the original OpenFAST model developed for the OC5/6 projects underpredicts the low-frequency surge force and pitch moment by 52% and 27%, respectively. With LC 5.3, the low-frequency surge and pitch resonance motions of the freely floating structure predicted by the new model are both within a 3% difference from the experimental measurements, showing a significant improvement from the original model, which underpredicts the surge and pitch resonance by 47% and 62%, respectively. With the blind validation using a white-noise wave (LC 3.4 and LC 5.4), the new model overpredicts the low-frequency surge force on the fixed structure by 35% and the surge resonance motion of the floating structure by 30%. In contrast, the original model underpredicts the low-frequency surge force by 36% but shows good agreement with the experiment in terms of the surge resonance motion with only a 3% difference. We consider the predictions by the new model acceptable, and it is very likely that they will be improved if the transverse drag coefficient near the waterline is slightly reduced, which was not done, in the spirit of a blind validation. With pitch, however, the new model shows significant improvements over the original model. The low-frequency pitch moment, previously underpredicted by 22% by the original model, is now within a 4% difference of the experiment with the new model. The improvement in the prediction of the low-frequency pitch motion is more significant with the original

model underpredicting by 49% and the new model giving a prediction within a 10% difference from the experiment. This improvement is achieved without having to retune the model parameters for the white-noise wave condition. Both the original and the new model give similar predictions for the wave-frequency loads and motion responses that are consistent with the experimental measurements.

The new model only introduces three new tunable parameters: the increased transverse drag coefficient near the waterline, the cutoff frequency of the high-pass velocity filter for computing the axial drag, and a scaling factor for the axial drag coefficient at low frequencies. As with any mid-fidelity model, some a priori information on the hydrodynamic characteristics of the floater from either experiments or high-fidelity CFD simulations is needed for model tuning; however, the fact that the model provides good predictions for the floater in white-noise waves without being specifically tuned for this condition demonstrates a degree of generalness of the model coefficients. We believe this is a nontrivial improvement over the existing mid-fidelity models used in the OC6 Phase I investigation, which, in general, were not able to match all low-frequency responses from the experiment at the same time. After further verification and validation, we plan to implement the proposed changes in a future version of OpenFAST as optional features to support the design and optimization of floating offshore wind platforms.

CRediT authorship contribution statement

Lu Wang: Conceptualization, Methodology, Software, Validation, Formal analysis, Investigation, Writing – original draft, Visualization. **Amy Robertson:** Conceptualization, Methodology, Investigation, Writing – review & editing, Supervision, Project administration, Funding acquisition. **Jason Jonkman:** Conceptualization, Methodology, Investigation, Writing – review & editing, Supervision. **Yi-Hsiang Yu:** Investigation, Writing – review & editing.

Declaration of competing interest

The authors declare that they have no known competing financial interests or personal relationships that could have appeared to influence the work reported in this paper.

Acknowledgements

This work was authored by the National Renewable Energy Laboratory, operated by Alliance for Sustainable Energy, LLC, for the U.S. Department of Energy (DOE) under Contract No. DE-AC36-08GO28308. Funding provided by the U.S. Department of Energy Office of Energy Efficiency and Renewable Energy Wind Energy Technologies Office. The views expressed in the article do not necessarily represent the views of the DOE or the U.S. Government. The U.S. Government retains and the publisher, by accepting the article for publication, acknowledges that the U.S. Government retains a nonexclusive, paid-up, irrevocable, worldwide license to publish or reproduce the published form of this work, or allow others to do so, for U.S. Government purposes.

References

- [1] A.N. Robertson, F. Wendt, J.M. Jonkman, W. Popko, H. Dagher, S. Gueydon, J. Qvist, F. Vittori, J. Azcona, E. Uzunoglu, et al., OC6 Project Phase II: validation of global loads of the DeepCwind floating semisubmersible wind turbine, *Energy Proc.* 137 (2017) 38–57, <https://doi.org/10.1016/j.egypro.2017.10.333>.
- [2] L.H.S. do Carmo, P.C. de Mello, E.B. Malta, G.R. Franzini, A.N. Simos, R.T. Gonçalves, H. Suzuki, Analysis of a FOWT model in bichromatic waves: an investigation on the effect of combined wave-frequency and slow motions on the calibration of drag and inertial force coefficients, in: ASME 39th International Conference on Ocean, Offshore and Arctic Engineering, 2020, <https://doi.org/10.1115/OMAE2020-18239>.
- [3] C. Lopez-Pavon, R.A. Watai, F. Ruggeri, A.N. Simos, A. Souto-Iglesias, Influence of wave induced second-order forces in semisubmersible FOWT mooring design, *J. Offshore Mech. Arctic Eng.* 137 (3) (2015), 031602, <https://doi.org/10.1115/1.4030241>.
- [4] F. Caillé, P. Bozonnet, T. Perdrizet, Y. Poirette, C. Melis, Model test and simulation comparison for an inclined-leg TLP dedicated to floating wind, in: ASME 36th International Conference on Ocean, Offshore and Arctic Engineering, 2017, <https://doi.org/10.1115/OMAE2017-61652>.
- [5] J. Azcona, F. Bouchotrouch, F. Vittori, Low-frequency dynamics of a floating wind turbine in wave tank-scaled experiments with SiL hybrid method, *Wind Energy* 22 (2019) 1402–1413, <https://doi.org/10.1002/we.2377>.
- [6] A. Robertson, E.E. Bachynski, S. Gueydon, F. Wendt, P. Schünemann, Total experimental uncertainty in hydrodynamic testing of a semisubmersible wind turbine, considering numerical propagation of systematic uncertainty, *Ocean Eng.* 195 (2020) 106605, <https://doi.org/10.1016/j.oceaneng.2019.106605>.
- [7] M. Fowler, 1/50-scale DeepCwind Semi-submersible Component Wave Testing, University of Maine, Advanced Structures and Composites Center, Orono, Maine, USA, 2021.
- [8] A. Robertson, L. Wang, OC6 Phase Ib: floating wind component experiment for difference-frequency hydrodynamic load validation, *Energies* 14 (19) (2021) 6417, <https://doi.org/10.3390/en14196417>.
- [9] A.N. Robertson, S. Gueydon, E. Bachynski, L. Wang, J. Jonkman, D. Alarcón, E. Amet, A. Beardsell, P. Bonnet, B. Boudet, et al., OC6 Phase I: Investigating the underprediction of low-frequency hydrodynamic loads and responses of a floating wind turbine, *J. Phys.: Conf. Ser.* 1618 (3) (2020), 032033, <https://doi.org/10.1088/1742-6596/1618/3/032033>.
- [10] L. Wang, A. Robertson, J. Jonkman, Y.-H. Yu, Uncertainty assessment of CFD investigation of the nonlinear difference-frequency wave loads on a semi-submersible FOWT platform, *Sustainability* 13 (1) (2021) 64, <https://doi.org/10.3390/su13010064>.
- [11] L. Wang, A. Robertson, J. Jonkman, Y.-H. Yu, A. Koop, A. Borràs Nadal, H. Li, W. Shi, R. Pinguet, Y. Zhou, Q. Xiao, R. Kumar, H. Sarlak, Investigation of nonlinear difference-frequency wave excitation on a semisubmersible offshore-wind platform with bichromatic-wave CFD simulations, in: ASME 3rd International Offshore Wind Technical Conference, 2021, <https://doi.org/10.1115/IOWTC2021-3537>.
- [12] L. Wang, A. Robertson, J. Jonkman, Y.-H. Yu, A. Koop, A. Borràs Nadal, H. Li, E. Bachynski-Polić, R. Pinguet, W. Shi, et al., OC6 Phase Ib: validation of the CFD predictions of difference-frequency wave excitation on a FOWT semi-submersible, *Ocean Eng.* 241 (2021) 110026, <https://doi.org/10.1016/j.oceaneng.2021.110026>.
- [13] I. Bayati, J. Jonkman, A. Robertson, A. Platt, The effects of second-order hydrodynamics on a semisubmersible floating offshore wind turbine, *J. Phys.: Conf. Ser.* 524 (1) (2014), 012094, <https://doi.org/10.1088/1742-6596/524/1/012094>.
- [14] F. Lemmer, W. Yu, P.W. Cheng, A. Pegalajar-Jurado, M. Borg, R.F. Mikkelsen, H. Bredmose, The Triplespar campaign: validation of a reduced-order simulation model for floating wind turbines, in: ASME 37th International Conference on Ocean, Offshore and Arctic Engineering, 2018, <https://doi.org/10.1115/OMAE2018-78119>.
- [15] M.I. Kvittem, P.A. Berthelsen, L. Eliassen, M. Thys, Calibration of hydrodynamic coefficients for a semi-submersible 10 MW wind turbine, in: ASME 37th International Conference on Ocean, Offshore and Arctic Engineering, 2018, <https://doi.org/10.1115/OMAE2018-77826>.
- [16] P.A. Berthelsen, R. Baarholm, C. Pákozdi, C.T. Stansberg, A. Hassan, M. Downie, A. Inceciik, Viscous drift forces and responses on a semisubmersible platform in high waves, in: ASME 28th International Conference on Ocean, Offshore and Arctic Engineering, 2009, <https://doi.org/10.1115/OMAE2009-79483>.
- [17] P.A. Berthelsen, E.E. Bachynski, M. Karimirad, M. Thys, Real-time hybrid model tests of a braceless semi-submersible wind turbine: Part III – calibration of a numerical model, in: ASME 35th International Conference on Ocean, Offshore and Arctic Engineering, 2016, <https://doi.org/10.1115/OMAE2016-54640>.
- [18] M. Böhm, A. Robertson, C. Hübler, R. Rolfs, P. Schaumann, Optimization-based calibration of hydrodynamic drag coefficients for a semisubmersible platform using experimental data of an irregular sea state, *J. Phys.: Conf. Ser.* 1669 (2020), 012023, <https://doi.org/10.1088/1742-6596/1669/1/012023>.
- [19] A.N. Simos, F. Ruggeri, R.A. Watai, A. Souto-Iglesias, C. Lopez-Pavon, Slow-drift of a floating wind turbine: an assessment of frequency-domain methods based on model tests, *Renew. Energy* 116 (2018) 133–154, <https://doi.org/10.1016/j.renene.2017.09.059>.
- [20] A. Pegalajar-Jurado, H. Bredmose, Reproduction of slow-drift motions of a floating wind turbine using second-order hydrodynamics and Operational Modal Analysis, *Mar. Struct.* 66 (2019) 178–196, <https://doi.org/10.1016/j.marstruc.2019.02.008>.
- [21] H. Li, E.E. Bachynski-Polić, Analysis of difference-frequency wave loads and quadratic transfer functions on a restrained semi-submersible floating wind turbine, *Ocean Eng.* 232 (2021) 109165, <https://doi.org/10.1016/j.oceaneng.2021.109165>.
- [22] H. Li, E.E. Bachynski-Polić, Validation and application of nonlinear hydrodynamics from CFD in an engineering model of a semi-submersible floating wind turbine, *Mar. Struct.* 79 (2021) 103054, <https://doi.org/10.1016/j.marstruc.2021.103054>.

- j.marstruc.2021.103054.
- [23] A.N. Robertson, E.E. Bachynski, S. Gueydon, F. Wendt, P. Schünemann, J. Jonkman, Assessment of experimental uncertainty for a floating wind semisubmersible under hydrodynamic loading, in: ASME 37th International Conference on Ocean, Offshore and Arctic Engineering, 2018, <https://doi.org/10.1115/OMAE2018-77703>.
- [24] C.-H. Lee, WAMIT Theory Manual, Massachusetts Institute of Technology, Department of Ocean Engineering, Cambridge, Massachusetts, USA, 1995. <http://wamit.com/Publications/tmanual.pdf>. (Accessed 23 July 2021).
- [25] W. Cummins, The Impulse Response Function and Ship Motion, David Taylor Model Basin, Washington, D.C., USA, 1962.
- [26] J. Jonkman, A. Robertson, G. Hayman, HydroDyn User's Guide and Theory Manual, National Renewable Energy Laboratory, Golden, Colorado, USA, 2014.
- [27] S. Gueydon, T. Duarte, J. Jonkman, Comparison of second-order loads on a semisubmersible floating wind turbine, in: ASME 33rd International Conference on Ocean, Offshore and Arctic Engineering, 2014, <https://doi.org/10.1115/OMAE2014-23398>.
- [28] S. Zhang, T. Ishihara, Numerical study of hydrodynamic coefficients of multiple heave plates by large eddy simulations with volume of fluid method, Ocean Eng. 163 (2018) 583–598, <https://doi.org/10.1016/j.oceaneng.2018.03.060>.
- [29] H. Li, E.E. Bachynski, Experimental and numerical investigation of nonlinear diffraction wave loads on a semi-submersible wind turbine, Renew. Energy 171 (2021) 709–727, <https://doi.org/10.1016/j.renene.2021.02.152>.
- [30] J.R. Chaplin, P. Teigen, Steady flow past a vertical surface-piercing circular cylinder, J. Fluid Struct. 18 (3–4) (2003) 271–285, <https://doi.org/10.1016/j.fluidstructs.2003.07.009>.
- [31] C. Clement, Investigation of Floating Offshore Wind Turbine Hydrodynamics with Computational Fluid Dynamics, Doctoral dissertation, University of Rouen Normandy, France, 2021.
- [32] F. Lemmer, W. Yu, P.W. Cheng, Iterative frequency-domain response of floating offshore wind turbines with parametric drag, J. Mar. Sci. Eng. 6 (4) (2018) 118, <https://doi.org/10.3390/jmse6040118>.
- [33] A.D. Boon, Drag of a Surface Piercing Cylinder in Fast Current and Low Waves, Master's thesis, Delft University of Technology, Netherlands, 2020.
- [34] H. Li, E.E. Bachynski-Polić, Experimental and numerically obtained low-frequency radiation characteristics of the OC5-DeepCwind semisubmersible, Ocean Eng. 232 (2021) 109130, <https://doi.org/10.1016/j.oceaneng.2021.109130>.
- [35] L. Wang, R.W. Yeung, An efficient hybrid integral-equation method for point-absorber wave energy converters with a vertical axis of symmetry, Appl. Ocean Res. 86 (2019) 195–206, <https://doi.org/10.1016/j.apor.2019.02.010>.
- [36] D. Son, V. Belissen, R.W. Yeung, Performance validation and optimization of a dual coaxial-cylinder ocean-wave energy extractor, Renew. Energy 92 (2016) 192–201, <https://doi.org/10.1016/j.renene.2016.01.032>.